J. Fluid Mech. (1997), *vol.* 345, *pp.* 251–286. Printed in the United Kingdom

Analysis of Monin–Obukhov similarity from large-eddy simulation

By SAMIR KHANNA AND JAMES G. BRASSEUR

Pennsylvania State University, University Park, PA 16802, USA

(Received 12 February 1996 and in revised form 24 February 1997)

A detailed analysis of the predictability of observed Monin–Obukhov (MO) similarity within the near-ground region of near-neutral to moderately convective atmospheric boundary layers (ABL) from large-eddy simulation (LES) fields is reported in this work. High-resolution LES predictions of means, variances, budgets of turbulent kinetic energy and temperature variance, and the velocity and temperature spectra from three ABL states ($-z_i/L = 0.44, 3$ and 8) are analysed under MO scaling. The resolution in the near-ground region is increased by using 'nested meshes.' For the close-to-neutral case ($-z_i/L = 0.44$) the relative roles of grid resolution and subgrid-scale (SGS) parameterization on the predictability of MO-similarity are also studied. The simulated temperature field is found to satisfy the MO hypothesis and agree well with observations. The simulated velocity field, on the other hand, shows significant departures. Except for the horizontal variance, MO scales are the appropriate normalizing scales for the near-ground-layer statistics. However, the LES suggest that the boundary layer depth z_i has an 'indirect' influence on all near-ground-layer variables except temperature, and the LES-predicted MO-scaled variables exhibit a functional dependence on both z/L and z/z_i. The simulated two-dimensional spectra of velocity and temperature fluctuations, however, suggest that while large scales deviate from MO-similarity, inertial subrange scales are MO-similar. Discrepancies with field observations raise important questions of the non-dimensional depth z/z_i over which MO-similarity holds for a particular variable. Surface-layer field studies generally do not document z_i. It is also not clear to what extent these discrepancies are due to approximations made in LES. Measurements are needed designed specifically for comparing with LES predictions.

1. Introduction

The Monin–Obukhov (MO) similarity hypothesis (Obukhov 1946; Monin & Obukhov 1954) implies that under horizontally homogeneous and quasi-stationary conditions the statistical structure of the near-ground region of an atmospheric boundary layer (ABL) is governed by only four parameters: $z, u_*, g/T_0$ and Q_0, where z is the distance from the ground, u_* is the surface friction velocity, g/T_0 is the buoyancy parameter and Q_0 is the surface temperature flux. These governing parameters form a single non-dimensional group z/L, where

$$L = \frac{-u_*^3}{k(g/T_0)Q_0} \tag{1.1}$$

is the Monin–Obukhov length scale and k is the von Kármán constant. Therefore, according to the MO hypothesis and dimensional analysis, statistical quantities non-

dimensionalized using the four governing parameters should be functions only of z/L in a layer adjacent to the ground. We distinguish between this 'MO layer' and the 'near-ground layer' which, in this study, we define as that region of the boundary layer where the vertical velocity integral length scale scales with the distance from the ground.

The Monin–Obukhov similarity hypothesis has been generally verified by experimental observations for several statistical moments (Businger *et al.* 1971; Wyngaard & Coté 1971; Kaimal *et al.* 1972; Panofsky *et al.* 1977; Kaimal 1978). Specifically, those moments that are dominated by vertical velocity fluctuations appear to scale on the four MO parameters. Horizontal turbulence motions, however, retain a strong influence from the outer buoyancy-induced large-scale eddying motions which scale on the boundary layer depth z_i (Panofsky *et al.* 1977).

Whereas in the past, field measurements provided the primary data to study atmospheric boundary layer (ABL) structure, large-eddy simulation (LES) (Deardorff 1970*a*, 1972, 1973) is now another important tool. Limited by the range of turbulence scales which can be captured on a computer, LES nevertheless provides full three-dimensional time-dependent predictions of all large-scale turbulence variables. However, with the exception of the ensemble-averaged horizontal velocity $U(z)$ and ensemble-averaged temperature $\Theta(z)$, there has been little attempt to analyse MO similarity using LES.

Studies by Mason & Thomson (1992) and Sullivan, McWilliams & Moeng (1994) have shown that the traditional Smagorinsky-style subgrid-scale (SGS) closures fail to predict the observed mean shear profile in the near-ground layer and have proposed certain modifications to the SGS parameterization to overcome this discrepancy. The Smagorinsky SGS parameterization is designed for LES of high-Reynolds-number turbulent flows where the large energy-containing motions are well resolved and the SGS motions begin well into the inertial range. For these conditions the Smagorinsky SGS closure causes a transfer of energy from resolved-scale to subgrid-scale motions such that the ensemble-mean energy transfer equals the ensemble-mean dissipation rate. In the ABL the size of the vertical velocity energy-containing eddies scales with the distance from the ground and therefore at some height LES fails to fully resolve the large-scale energy-containing vertical motions in the near-ground region. Mason & Thomson (1992) proposed that the local transfer of energy from subgrid- to resolved-scale motions, 'back scatter', becomes significant when the large scales are not fully resolved. In their simulation of the neutral planetary boundary layer, Mason & Thomson included a stochastic 'back scatter' of energy that resulted in a significant improvement of the mean shear profile. Sullivan *et al.* (1994) modified the SGS parameterization such that in the limit where all the turbulent motions are unresolved, the SGS stresses approach the ensemble-mean turbulent stresses. Sullivan *et al.* showed a marked improvement in the mean shear profiles of neutral and close-to-neutral ($-z_i/L = 0.5$) ABLs.

The studies of Mason & Thomson and Sullivan *et al.* demonstrated the need for improved SGS parameterization to predict the observed mean wind and temperature profiles in the near-ground region. The extent to which other statistical moments agree with observation, however, is not known. Even less well understood are the relative roles of grid resolution and SGS parameterization on LES predictions of all relevant statistics.

Monin–Obukhov similarity is a near-ground phenomenon and a detailed analysis of higher-order moments and local structure with LES requires the ability to capture integral-scale motions which scale on z. As pointed out, however, the grid resolution at

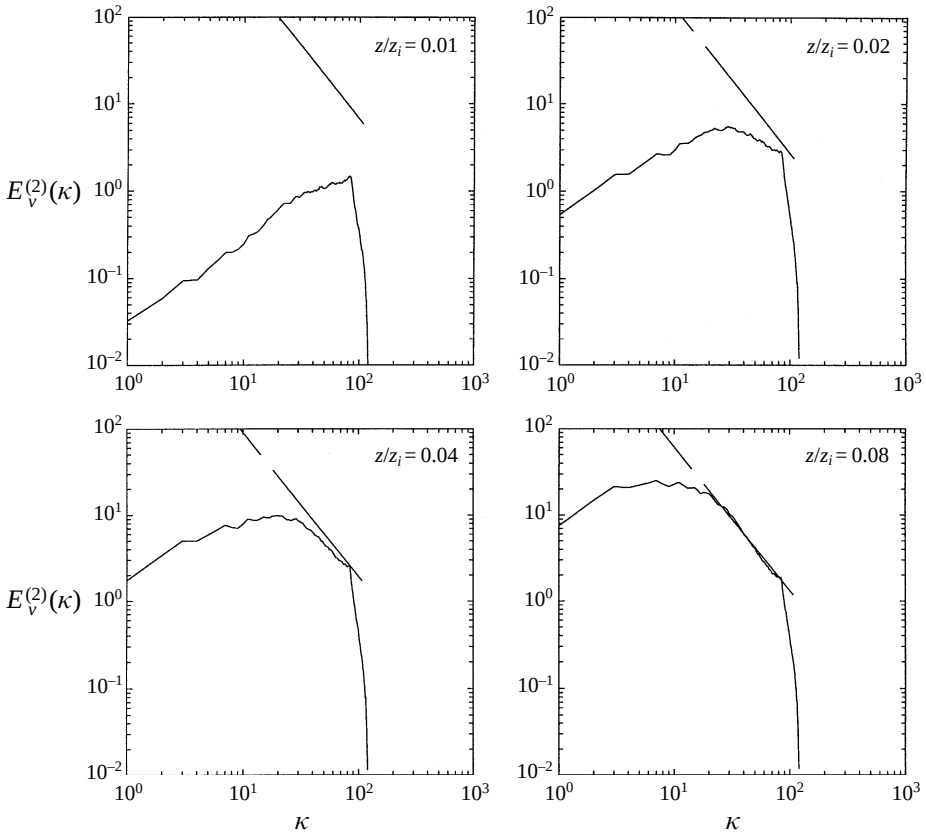

FIGURE 1. Two-dimensional vertical velocity spectra from effective 256^3 embedded mesh simulation at $-z_i/L = 8$ (details of the simulation are in §3). The dashed line is inertial-range prediction (equation (6.12)).

the first few grid levels is always insufficient to capture the energy-containing vertical motions. Figure 1, for example, for the vertical velocity spectra at different heights obtained from our 'embedded mesh', shows the transition from the under-resolved region adjacent to the ground, where the peak in the spectrum is not captured, to a well-resolved region away from the ground, where the filter-cutoff wavenumber lies in the inertial subrange. It is not clear how this under-resolved region affects the prediction of near-ground regions that are well resolved. Hibberd & Sawford (1994) observed some discrepancies between the LES-predicted mixed-layer statistics in a convective boundary layer and the measurements in a laboratory tank experiment. To study the effects of grid resolution and to reduce the under-resolved region, we employ an 'embedded mesh' technique whereby a fine mesh covering a fraction of the boundary layer depth is embedded adjacent to the ground within a coarse mesh covering the entire computational domain. The details of this strategy and the numerical simulations are provided in §3.

In this study we analyse the ability of LES to capture elements of MO similarity. In §4 we study the relative roles of SGS parameterization and grid resolution on LES predictions of mean shear, mean temperature gradient and vertical velocity variance of a close-to-neutral ABL ($-z_i/L = 0.44$). In particular, we compare two SGS parameterizations, Moeng (1984) and Sullivan *et al.* (1994), and two grid resolutions,

$-z_i/L$	L_x (m)	L_y (m)	L_z (m)	Q_0 (m s^{-1} K^{-1})	U_g (m s^{-1})	z_i (m)
0.44	3000	3000	1000	0.01	15	525
3	5000	5000	2000	0.06	15	1060
8	5000	5000	2000	0.24	15	1020

TABLE 1. Global parameters of the three ABL states analysed. L_x, L_y and L_z are the streamwise, cross-stream and vertical extents of the computational domain, respectively; Q_0 is the surface temperature flux; U_g is the geostrophic wind speed; and z_i is the height of the capping inversion.

128^3 and an effective 256^3 'embedded mesh.' With a conclusion that an effective 256^3 'embedded mesh' simulation with the Sullivan *et al.* SGS parameterization gives predictions in closer agreement with experimental observations, we analyse in detail the corresponding $-z_i/L = 0.44, 3$ and 8 simulations under MO scaling. Table 1 summarizes the global parameters for these cases. The horizontal extent of the domain is roughly 15 times the maximum horizontal-integral length scale of the vertical velocity fluctuations, sufficient to resolve a few integral-scale eddies. The choice of domain size was based on previous LES studies (see for example Deardorff 1972; Moeng 1984; Schmidt & Schumann 1989). Statistics were calculated by averaging over horizontal planes and a few time steps. The results for temperature statistics are presented in §5 and those for velocity statistics are presented in §6.

2. MO-similarity, field measurements and LES

Large-eddy simulation is a powerful tool in the study of local as well as statistical structure of the atmospheric boundary layer. However, LES faces certain challenges, particularly in the near-ground region, and needs to be used in close conjunction with field measurements (see for example Wyngaard & Peltier 1995) in order to analyse its potentials and weaknesses. In this study we make close comparisons of our LES results with field measurements. However, there are certain fundamental differences between data available from LES and data available from field measurements that are important to consider when comparing near-ground-layer statistics and MO-similarity.

Monin–Obukhov similarity provides a framework for organizing the statistical structure of the near-ground region of an ABL under various stability states. There are two issues involved in this similarity approach: the choosing of the appropriate scales for *normalizing* statistical variables, and the determination of the functional dependence of a normalized variable on other non-dimensional parameters. Normalization implies that the dimensionless variable be of $O(1)$. According to the MO hypothesis, z is the only appropriate length scale, u_* is the only appropriate velocity scale and $T_* = -Q_0/u_*$ is the only appropriate temperature scale which normalizes near-ground-layer variables. Statistical quantities in the near-ground region when non-dimensionalized by these scales should be $O(1)$ quantities. The MO hypothesis further assumes that z, u_*, Q_0, and g/T_0 are the *only* significant parameters which statistically characterize the near-ground region. Hence the appropriately normalized quantities should be functions of the only non-dimensional group z/L, that is

$$\frac{f}{f_{MO}} = \Phi_f\left(\frac{z}{L}\right), \tag{2.1}$$

where f is some statistical quantity of interest and f_{MO} is the corresponding MO scale.

In the free convection limit ($-z_i/L = \infty$), u_* and L are no longer relevant scales and the characteristic near-ground-layer velocity scale is given by

$$u_f = \left(k\frac{g}{T_0}Q_0 z\right)^{1/3}. \tag{2.2}$$

In the absence of any influence from the boundary layer depth z_i, statistical quantities normalized by the remaining MO parameters are constant. As $-z_i/L \to \infty$, then, MO-similarity within the near-ground layer approaches 'local free convection' similarity with z and $u_f(z)$ as the relevant length and velocity scales (Wyngaard, Coté & Izumi 1971; Wyngaard & Coté 1972).

In the neutral limit ($-z_i/L = 0$), $Q_0\ g/T_0$ and L are no longer relevant scales. In the absence of any influence from the boundary layer depth z_i, statistical quantities normalized by the remaining MO parameters are constant. As $-z_i/L \to 0$, then, MO-similarity within the near-ground layer approaches 'local neutral' similarity with z and u_* as the relevant length and velocity scales.

Influences that introduce other relevant scales not included in the MO hypothesis, such as motions which scale on the boundary layer depth z_i or the fluxes of momentum and heat at the upper interface, could cause deviations from statistical similarity. The boundary layer depth z_i has perhaps the greatest potential for influencing the near-ground layer through the near-ground sweeping motions from mixed-layer eddies that scale on z_i. These mixed-layer eddies have a characteristic velocity scale $w_* = (g/T_0 Q_0 z_i)^{1/3}$. The boundary layer depth can either have a 'direct' influence on the near-ground-layer statistics, in that the dominant normalizing scales are the mixed-layer scales ($z_i, w_*, \theta_* = -Q_0/w_*$, observed by Deardorff 1970*b*), or have an 'indirect' influence wherein the appropriate normalizing scale is still the MO scale but z_i must be included in the list of governing parameters to determine the functional dependence of the normalized variables. When z_i is included in the list of the parameters which statistically characterize the near-ground region, the normalized quantities will be functions of two independent non-dimensional groups: z/L and z/z_i and (2.1) must be modified to:

$$\frac{f}{f_{MO}} = \Phi'_f\left(\frac{z}{L}, \frac{z}{z_i}\right). \tag{2.3}$$

LES provides height-dependent statistics of resolved-scale variables with a SGS contribution estimated from SGS parameterization for nearly the entire boundary-layer depth. Profiles obtained for different stability states z_i/L can be plotted as a function of z/L or z/z_i. Therefore, it is useful to express (2.3) equivalently as

$$\frac{f}{f_{MO}} = \Phi''_f\left(\frac{z}{L}, \frac{z_i}{L}\right) \tag{2.4}$$

or

$$\frac{f}{f_{MO}} = \Phi'''_f\left(\frac{z}{z_i}, \frac{z_i}{L}\right). \tag{2.5}$$

If the influence of z_i in determining the functional dependence is small, equations (2.3) and (2.4) reduce to equation (2.1). On the other hand, if the influence of z_i is dominant then a better collapse of an MO-normalized variable will be obtained when plotted as a function of z/z_i. If the 'indirect' influence of z_i is significant but not dominant, forms (2.4) or (2.5) are appropriate.

In the past, attempts have been made to verify MO-similarity (2.1) with field observations, generally with measurements at a few heights close to the ground (typically < 30 m) and under various stability states (z_i/L). Businger *et al.* (1971) verified MO-similarity for mean shear and mean temperature gradient and determined the respective functional relationships Φ_m and Φ_h, Wyngaard & Coté (1971) analysed the budgets of turbulent kinetic energy and temperature variance under MO scalings, Panofsky *et al.* (1977) tested the hypothesis for velocity variances, and Kaimal *et al.* (1972) (see also Kaimal *et al.* 1976 and Kaimal 1978) analysed the MO-normalized velocity and temperature spectra. Recently, Högström (1990) and Kader and Yaglom (1990) have summarized various field observations of the statistical structure of the near-ground region.

Measurements of Panofsky *et al.* (1977) revealed that while vertical velocity fluctuations do observe MO-similarity in the near-ground region, horizontal velocity fluctuations scale with mixed-layer parameters. This scaling of horizontal fluctuations was also predicted in the numerical simulations of Deardorff (1973) and the laboratory tank experiments of Willis & Deardorff (1974). A physically plausible explanation for these non-local effects of mixed-layer scales on surface-layer eddies is given by Hunt, Kaimal & Gaynor (1984) and Hunt *et al.* (1988) who argue that the large thermal plumes are formed in the mixed-layer and that these plumes effectively act as non-Gaussian free-stream turbulence in the surface layer. Measurements of Banta (1985) have demonstrated that the departure of horizontal fluctuations from MO-similarity is due to the mixed-layer convective eddies that sweep the near-ground region. Wyngaard (1988) has shown that the horizontal velocity fluctuations can be expressed in the form (2.3). Wyngaard (1988) also provides a historical perspective and the present understanding of MO-similarity and near-ground region.

While the field measurements have tested the hypothesis to a large extent, some issues, primarily from the LES perspective, remain unresolved. Most importantly, the field measurements do not always provide the boundary layer depth z_i making it impossible to determine the ranges of non-dimensional depth z/z_i over which MO-similarity, for the variables measured, is valid. Our rough estimates of z_i suggest that most of these measurements are likely to be in the range $z/z_i < 0.03$. This is a rather narrow range given that the near-ground layer is typically quoted (see for example Kaimal *et al.* 1976) to extend to $z/z_i \approx 0.1$. However, practical limitations on tower height make it difficult to measure at larger z/z_i. Above $z/z_i \approx 0.03$ available data lie in the mixed layer ($z/z_i > 0.2$) making it difficult to study the transition from near-ground-layer to mixed-layer scalings. As a result, it is not known to what relative height, z_{MO}/z_i, MO-similarity applies for any particular statistical variable f and for any particular atmospheric state, $-z_i/L$. Nor do we know how the 'MO layer' z_{MO}/z_i for a variable f varies with stability state z_i/L.

Note that we distinguish between the 'near-ground layer' $0 < z/z_i < z_s/z_i$, defined here as the layer adjacent to the ground where the vertical velocity integral scale scales on z, and the 'MO layer' $0 < z/z_i < z_{MO}/z_i$, defined as the layer in which a statistical variable collapses under MO scaling. This differentiation is illustrated in figure 2. Note that $z_{MO}/z_i \leqslant z_s/z_i$ and that, in general, both z_{MO}/z_i and z_s/z_i vary with $-z_i/L$, although not necessarily together. In addition, z_{MO}/z_i depends on the statistical variable f. For $L \ll z_s$ Kader & Yaglom (1990) discuss the transition from shear-dominated MO scaling to local free-convection scaling. For the neutral to moderately convective boundary layers considered here, L is either larger than or of the order of z_s.

Although LES provides data to analyse the near-ground region and the transition

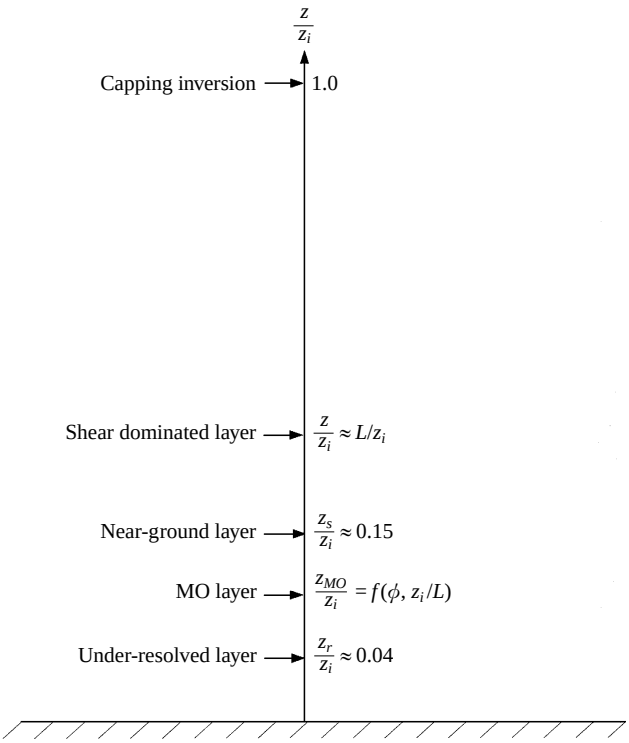

FIGURE 2. Schematic illustration of the various regions relevant for Monin–Obukhov analysis of a statistical variable ϕ from LES data.

from near-ground-layer to mixed-layer scaling, the simulations give only the resolved-scale fields. As a result, the SGS contribution to any statistical variable must be estimated. When the resolved scales extend well into the inertial subrange, the SGS contributions are small and the statistics are relatively insensitive to SGS estimates. However, LES fails to resolve well inertial-subrange scales at the first few grid points, restricting the height z_r above which the simulations are 'well-resolved.' Below this height, SGS effects make significant contributions to large-scale statistics and their estimates are important. The smallest height z_1/z_i in our 256^3 'embedded mesh' simulations is ≈ 0.008 and based on the spectrum at various heights (e.g. figure 1) we estimate z_r/z_i to be ≈ 0.04. Below z_r, SGS estimates are questionable and our results should be viewed with caution.

Figure 2 summarizes these issues in a schematic of the various regions in a large-eddy simulation of an ABL. Note especially that the available near-ground-layer data from field observations is mostly at heights lower than z_r making it difficult to verify LES predictions. If the depth of the MO layer (z_{MO}) for a given variable f (unknown) is higher than z_r, LES should be able to capture MO-similarity in the region $z_r/z_i \leqslant z/z_i \leqslant z_{MO}/z_i$. In our analysis, we present MO-normalized profiles of various statistics obtained from a 256^3 embedded mesh simulation of the convective boundary layer for three stability states, $-z_i/L = 0.44, 3$ and 8, as a function of z/L. If MO-similarity (2.1) strictly holds, these profiles should collapse onto a single curve. To explore deviations from strict MO-similarity, we explore also form (2.3), and possible scaling by the outer scales.

3. Numerical simulations

We use a modified version of Moeng's LES algorithm (described by Moeng 1984) to simulate the ABL, described briefly in §3.1. The original algorithm was modified to incorporate an improved SGS parameterization proposed by Sullivan *et al.* (1994) (§3.2) and to incorporate an embedded mesh strategy (§3.3).

3.1. *The LES algorithm*

Moeng's algorithm solves the filtered Navier–Stokes equation,

$$\frac{\partial u_i^r}{\partial t} = \epsilon_{ijk} u_j^r \omega_k^r - \frac{\partial P^*}{\partial x_i} - \frac{\partial \overline{P}}{\partial x_i} + \frac{g}{\Theta_0}\Theta^r \delta_{i3} + \epsilon_{ij3} f u_j^r - \frac{\partial \tau_{ij}}{\partial x_j}, \tag{3.1}$$

where f^r is a 'resolved-scale' variable obtained by filtering the full field f:

$$f^r(\boldsymbol{x}, t) = \int G(\boldsymbol{x} - \boldsymbol{y}) f(\boldsymbol{y}, t) \mathrm{d}\boldsymbol{y}. \tag{3.2}$$

The filter $G(x_i)$ determines the scales resolved by the simulations. The 'subgrid-scale' variable is given by

$$f^s = f - f^r. \tag{3.3}$$

In (3.1) u_i^r and ω_i^r are the resolved-scale velocity and vorticity fields. P^* is a modified resolved-field normal stress given by

$$P^* = \frac{p^r}{\rho_0} + \frac{R_{kk}}{3} + \frac{(u_k^r u_k^r)^r}{2}, \tag{3.4}$$

where p^r is the filtered fluctuating pressure field, ρ_0 is the density of the motionless adiabatic base state and R_{ij} describes the interaction between the resolved- and subgrid-scale velocity fields,

$$R_{ij} = (u_i^r u_j^s + u_i^s u_j^r + u_i^s u_j^s)^r. \tag{3.5}$$

The mean constant pressure gradient, $\partial \overline{P}/\partial x_i$, is prescribed in the simulations. The fourth term on the right-hand side of (3.1) is the resolved buoyancy force, where Θ^r is the deviation in resolved potential temperature from the motionless adiabatic base state Θ_0. The next term is the Coriolis force, f is the Coriolis parameter. Finally, τ_{ij} is the 'SGS stress tensor' given by the deviatoric part of R_{ij}:

$$\tau_{ij} = R_{ij} - R_{kk}\delta_{ij}/3, \tag{3.6}$$

and is parameterized using a SGS closure.

The continuity constraint

$$\frac{\partial u_i^r}{\partial x_i} = 0 \tag{3.7}$$

is used to derive the Poisson equation for P^*:

$$\nabla^2 P^* = \frac{\partial H_i}{\partial x_i}, \tag{3.8}$$

where H_i is the right-hand side of (3.1) without $\partial P^*/\partial x_i$.

The equation governing Θ^r is

$$\frac{\partial \Theta^r}{\partial t} = -\frac{\partial u_i^r \Theta^r}{\partial x_i} - \frac{\partial Q_i}{\partial x_i}, \tag{3.9}$$

where Q_i is the SGS potential temperature flux given by

$$Q_i = (\Theta^r u_i^s + \Theta^s u_i^r + \Theta^s u_i^s)^r. \tag{3.10}$$

Equations (3.1), (3.8) and (3.9) are solved in a computational domain (L_x, L_y, L_z) using uniformly spaced grid points (N_x, N_y, N_z). The vertical height of the computational domain (L_z) is approximately twice the boundary-layer depth z_i, and the horizontal domain $(L_x \times L_y)$ is about $5z_i \times 5z_i$ in our simulations. The simulated ABL is horizontally homogeneous. Consequently, the horizontal directions (x, y) are advanced pseudo-spectrally, while vertical derivatives are approximated with second-order central differences. The grid planes are staggered in the vertical with the first vertical velocity plane a distance Δz from the surface, and the first horizontal velocity and temperature plane at $\Delta z/2$ from the surface.

Finite differencing in the vertical requires boundary conditions at the surface. The resolved velocity field satisfies no-slip at the surface while $\Theta^r(z = 0)$ is derived from the value at the first grid point using the MO-similar profile given by Paulson (1970). The surface values of SGS stresses are evaluated from the velocity field at the first grid point using a local drag law

$$\tau_{i3} = C_D S u_i^r, \tag{3.11}$$

where S is the wind speed at the first grid point. C_D is the drag coefficient given by

$$C_D = \frac{u_*^2}{\overline{S}^2}, \tag{3.12}$$

where an overbar denotes ensemble mean. The kinematic wall stress, $u_*^2 = -\overline{uw}(z = 0)$, is evaluated from the velocity field at the first grid point using the MO-similar profile given by Paulson (1970). At the upper boundary of the grid ($z \approx 2z_i$) the vertical velocity is set to 0 and the vertical gradients of horizontal velocity and potential temperature are fixed.

Time is advanced using a second-order explicit Adams–Bashforth scheme where a variable f is evaluated at a future time step $n + 1$ from

$$f^{n+1} = f^n + C\Delta t R^n + (1 - C)\Delta t R^{n-1}, \tag{3.13}$$

where R is the right-hand side of (3.1) or (3.9), Δt is the time step and $C = 1.5$ in the current simulations.

3.2. *Subgrid-scale parameterizations*

Moeng (1984) uses a Smagorinsky-style SGS closure:

$$\tau_{ij} = -2\nu_t S_{ij}^r, \tag{3.14}$$

$$Q_i = -\nu_\theta \frac{\partial \Theta^r}{\partial x_i}, \tag{3.15}$$

where S_{ij}^r is the resolved-scale strain rate, $\frac{1}{2}(\partial u_i^r/\partial x_j + \partial u_j^r/\partial x_i)$, and ν_t and ν_θ are the SGS eddy-viscosity coefficients for momentum and temperature, respectively. The eddy-viscosity coefficients are evaluated from velocity and length scales characterizing the SGS motions:

$$\nu_t = 0.1 l\, e^{1/2}, \tag{3.16}$$

$$\nu_\theta = [1 + (2l/\Delta s)]\nu_t, \tag{3.17}$$

where l is the SGS length scale, e is the resolved SGS energy determined from a separate prognostic equation and $\Delta s = (\Delta x \Delta y \Delta z)^{1/3}$.

The length scale l is taken to be Δs when the stratification is negative (i.e. $\partial \Theta^r / \partial z < 0$) and

$$l = l_s = 0.76 e^{1/2} \left(\frac{g}{\Theta_0} \frac{\partial \Theta^r}{\partial z} \right)^{-1/2} \tag{3.18}$$

when the stratification is positive and $l_s < \Delta s$.

Sullivan *et al.* (1994) recognized that the SGS formulation above yields a mean velocity profile inconsistent with observations (and MO-similarity) and proposed the following modification to (3.14):

$$\tau_{ij} = -2\gamma \nu_t S^r_{ij} - 2\nu_T \overline{S}_{ij}. \tag{3.19}$$

Thus equation (3.19) forces τ_{ij} to approach the Prandtl mixing-length formulation for turbulent stresses as the grid resolution becomes very poor near the ground while maintaining the Smagorinsky form away from the ground and in regions of low mean strain rate. In principle, a proper SGS parameterization should have this feature built-in and there should not be a need for another term. Equation (3.19), nevertheless, shows improvements in the mean shear profile and was used in this study.

The eddy-viscosity coefficient $\nu_T(z)$ in (3.19) is specified a decreasing function of z evaluated at the ground by constraining the mean shear at the first vertical velocity level to the MO-similar form proposed by Businger *et al.* (1971). The 'isotropy factor' γ is given by

$$\gamma = \frac{S'}{S' + \overline{S}}, \tag{3.20}$$

where S' is the horizontally averaged fluctuating resolved strain

$$S' = \left[\overline{2(S^r_{ij} - \overline{S_{ij}})(S^r_{ij} - \overline{S_{ij}})} \right]^{1/2} \tag{3.21}$$

and $\overline{S}$ is the mean strain

$$\overline{S} = \left(2\overline{S^r_{ij} S^r_{ij}} \right)^{1/2}. \tag{3.22}$$

The isotropy factor reduces the first term in (3.19) at small z where resolution is poor and S^r_{ij} is not far from its ensemble mean value $\overline{S^r_{ij}}$. In the mixed layer $\nu_T \overline{S_{ij}} \approx 0$ and $\gamma \approx 1$.

3.3. *Resolution and embedded mesh*

To improve the resolution in the near-ground layer we apply an embedded mesh strategy whereby a fine mesh covering a fraction of the boundary layer depth is embedded within a coarser mesh covering the entire computational domain. The simulations on the two meshes are run independently except that the upper boundary condition for the fine mesh is obtained from the coarse mesh.

Figure 3 illustrates the fine-mesh/coarse-mesh interface where the upper boundary conditions for the fine mesh are applied. The vertical velocity (w) and SGS energy (e) at the upper extremity of the fine mesh (NF_w) coincide with a vertical velocity and SGS energy on the coarse mesh (NC_w) at a height z where the coarse mesh simulation resolves well into the inertial subrange. Because the grids are staggered in the vertical with uniform spacing, the topmost fine-mesh horizontal velocity (u, v) and temperature (Θ) level (NF_u, which lies below the NF_w level) lies above the closest

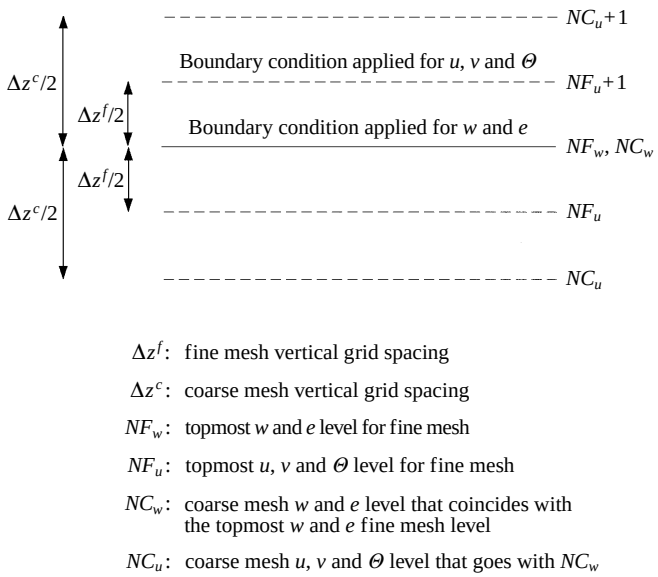

FIGURE 3. Illustration of the interface between the coarse mesh and the embedded fine mesh. The solid line is the w and e level whereas the dashed line is the u, v, Θ level.

(u, v, Θ) level on the coarse grid (NC_u). The boundary conditions for the fine mesh are obtained from the coarse mesh at $NF_w \equiv NC_w$ and $NF_u + 1$, which must be interpolated from coarse mesh values at NC_u and $NC_u + 1$.

To satisfy the Courant condition, the time step used for the fine mesh is smaller than the time step used for the coarse mesh. Thus both spatial and temporal interpolations are required in specifying the fine mesh boundary conditions from the coarse mesh results. Linear interpolation is used for (u, v, Θ) in the vertical and for all variables in time. The horizontal interpolations are done in Fourier space. Because the fine mesh resolves smaller-scale motions than the coarse mesh, it is necessary to extend the horizontal wavenumbers of (u, v, w, Θ, e) into the range $k_x^c < k_x \leqslant k_x^f$ and $k_y^c < k_y \leqslant k_y^f$, where the superscripts c and f represent the cutoff wavenumbers on the coarse and fine meshs, respectively. These Fourier modes were assigned an amplitude given by extending the Kolmogorov $k^{-5/3}$ spectra, and a random phase.

The upper boundary condition for P^* must be specified at NF_u (see figure 3). This condition is derived using continuity at NF_u which at time step $n+1$ implies

$$\frac{\partial}{\partial x}\left(u|_{NF_u}^{n+1}\right) + \frac{\partial}{\partial y}\left(v|_{NF_u}^{n+1}\right) + \frac{w|_{NF_w}^{n+1} - w|_{NF_w-1}^{n+1}}{\Delta z} = 0, \tag{3.23}$$

where $|_N^n$ represents the value of a variable at time step n and level N and central differences are applied in the vertical. The upper boundary condition for the fine mesh provides $w|_{NF_w}^{n+1}$. Substituting expression (3.13) for $u|_{NF_u}^{n+1}, v|_{NF_u}^{n+1}$ and $w|_{NF_w-1}^{n+1}$ and writing the right-hand sides R_i of (3.1) at time step n as a sum of the pressure gradient term and a remainder H_i, yields

$$-\frac{\partial}{\partial x^2}\left(P^*|_{NZ_u}^n\right) - \frac{\partial}{\partial y^2}\left(P^*|_{NZ_u}^n\right) + \frac{1}{\Delta z}\frac{\partial}{\partial z}\left(P^*|_{NZ_w-1}^n\right) = g, \tag{3.24}$$

where g is known. Equation (3.24) serves as the upper boundary condition for P^*.

The SGS energy should decrease with the increase in resolution from the coarse

to fine mesh at NF_w. To account for this decrease, an approximation proposed by Sullivan and Moeng (personal communication) is made where the local flux of energy from the resolved to the subgrid scales, S, is related to the SGS energy and largest subgrid length scale l by the local Kolmogorov relationship

$$S \propto \frac{e^{3/2}}{l}. \tag{3.25}$$

Assuming that both fine and coarse grid resolutions are within the inertial subrange,

$$e_f = e_c \left[\frac{l_f}{l_c}\right]^{2/3}, \tag{3.26}$$

where l_f/l_c is the ratio of cell lengths in the fine and coarse grids. Equation (3.26) is used to specify the SGS energy upper boundary condition for the fine mesh simulation from the coarse mesh results.

In our approach there is a one-way communication from the coarse mesh to the fine mesh through the upper boundary condition, an approach developed in collaboration with Dr Peter Sullivan of NCAR. Recently Sullivan and Moeng have developed a 'nested-mesh' algorithm with two-way communication between the coarse and the fine meshes.

To test the accuracy of our embedded mesh algorithm, two simulations were carried out for a moderately convective ABL ($-z_i/L = 8$): a 192^3 simulation covering the entire computational domain, and a 128^3 simulation covering the entire domain with an effective 192^3 embedded mesh covering one quarter of the boundary layer depth ($0.25z_i$). The initial conditions for the two simulations were obtained from the 128^3 full simulation and all simulations used the Moeng (1984) SGS parameterization. In preliminary calculations, we observed a build-up of turbulent kinetic energy in the u and the v components at the upper interface of the embedded mesh which was insensitive to the type of interpolation approximation used. To control this spurious increase in turbulent kinetic energy, the flux of energy from the resolved to the subgrid scales at the upper interface of the embedded mesh was artificially enhanced by increasing the constant in (3.16) from 0.1 to 0.2 at the level NF_w only (see figure 3). The agreement between the 192^3 simulation and the effective 192^3 embedded-mesh simulation with the SGS constant adjusted at the upper interface is very good. Figure 4, for example, shows the r.m.s. of the fluctuating velocity and potential temperature from these two simulations after approximately one-half a mixed-layer eddy-turnover time $\tau = z_i/w_*$.

The three-dimensional instantaneous local structure as obtained from the two simulations also agrees very well. Figure 5 shows a streamwise view of isosurfaces of vertical velocity fluctuations at a positive threshold level near w_*. These regions of strong upward velocity fluctuations represent the 'updraughts' or 'plumes' in a convective boundary layer responsible for most of the upward flux of momentum, heat or passive scalar (Moeng & Wyngaard 1984 and Schmidt & Schumann 1989). Figure 5(a) shows the updraughts in the 128^3 simulation which had an effective 192^3 embedded mesh in the near-ground region. Figure 5(b) shows the updraughts in a 192^3 simulation after one half τ beginning with the same initial conditions as the 128^3 embedded mesh simulation. A comparison of these two figures shows the improvement in structural detail that is obtained by increased resolution. The merging of small plumes near the surface that is so evident in the 192^3 simulation is not as apparent in the 128^3 simulation. The near-ground region of the 192^3 simulation is

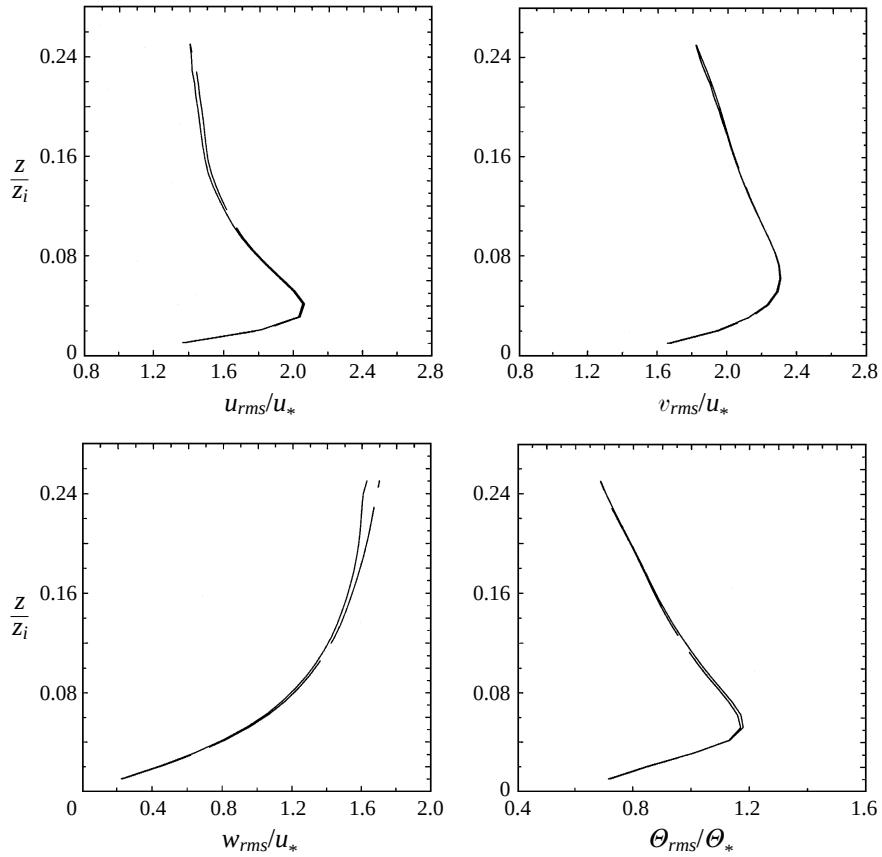

FIGURE 4. Root-mean-square profiles obtained from two simulations: solid line from full 192^3 simulation and dashed line from effective 192^3 embedded mesh simulation with the SGS constant adjusted at the upper interface (see text).

replotted in figure 5(*c*) for comparison with the local structure obtained from the effective 192^3 embedded mesh simulation in figure 5(*d*). The agreement between figures (*c*) and (*d*) is very good, demonstrating the ability of the embedded mesh strategy to capture the local dynamics of the near-ground region at higher resolution.

4. Effects of grid resolution and SGS parameterization

To study the effects of grid resolution and SGS parameterization on LES predictions of MO-similarity, we compare mean gradients and vertical velocity variance using two SGS parameterizations and two grid resolutions with the field measurements of Businger *et al.* (1971) and Panofsky *et al.* (1977). Specifically we compare the SGS parameterizations of Moeng (1984, hereafter called M84) and Sullivan *et al.* (1994, hereafter called SMM94), and we apply 128^3 and effective 256^3 embedded mesh grid resolutions for a simulation of a close-to-neutral ABL ($-z_i/L = 0.44$).

If MO-similar, mean shear is given by

$$\frac{kz}{u_*}\frac{\partial U}{\partial z} = \Phi_m\left(\frac{z}{L}\right), \tag{4.1}$$

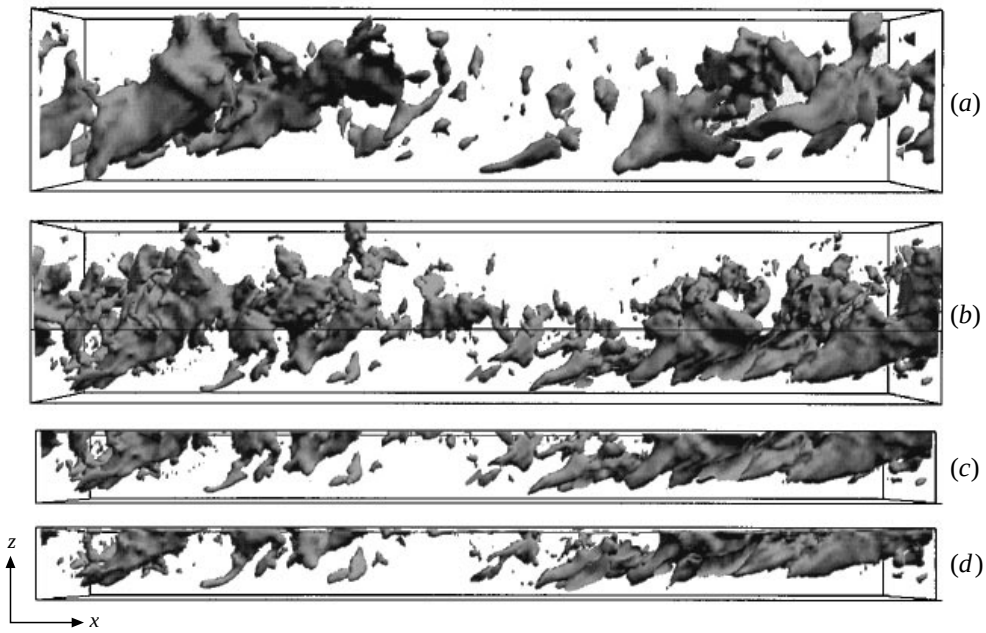

FIGURE 5. Isosurfaces of vertical velocity fluctuations (w) in $z_i/L = 8$ case: (a) 128^3 simulation, (b) 192^3 simulation, (c) near-ground region from the 192^3 simulation, (d) near-ground region from the effective 192^3 embedded mesh simulation.

where $[\partial U/\partial z]_{MO} = u_*/kz$ (equation (2.1)), $k = 0.4$ being the von Kármán constant. From field measurements Businger *et al.* (1971) developed the following empirical relationship for the non-dimensional mean shear Φ_m:

$$\Phi_m\left(\frac{z}{L}\right) = \left(1 - 15\frac{z}{L}\right)^{-1/4}. \tag{4.2}$$

Figure 6(a) shows the MO-normalized mean shear profiles obtained from the two SGS parameterizations and two grid resolutions along with (4.2). The 128^3 simulation using M84 (curve D) greatly over predicts the mean shear measured by Businger *et al.* The SMM94 parameterization (curve B) shows a marked improvement in the agreement between LES prediction and field observations. Whereas increasing the resolution improves the agreement using both SGS schemes (curves A and C), the agreement using M84 (curve C) remains unsatisfactory. Away from the surface where the M84 and the SMM94 parameterizations coincide, both schemes give similar predictions when LES resolves well into the inertial subrange. Near the ground shear is always over predicted. Whereas the magnitude of the overshoot is sensitive to the SGS parameterization, increased resolution moves the overshoot closer to the ground suggesting that poor resolution at the first couple of levels (figure 1) is always a significant source of imprecision that affects the solution at higher z.

MO-similarity of mean potential temperature gradient implies

$$\frac{kz}{T_*}\frac{\partial \Theta}{\partial z} = \Phi_h\left(\frac{z}{L}\right). \tag{4.3}$$

Businger *et al.* (1971) developed the following empirical relationship for the non-

dimensional mean temperature gradient Φ_h:

$$\Phi_h\left(\frac{z}{L}\right) = 0.74\left(1 - 9\frac{z}{L}\right)^{-1/2}. \tag{4.4}$$

Later field measurements suggest a coefficient of 0.9 instead of 0.74 in (4.4), see Kader & Yaglom (1990) for a review. Figure 6(*b*) compares (4.4), with the adjusted coefficient, with the MO-normalized mean potential temperature gradient profiles obtained from the two SGS parameterizations and two grid resolutions. Whereas major improvement results from the SMM94 SGS model, increased resolution acts primarily to move the maximum deviations closer to the ground.

Hunt & Graham (1978) show that in wall-bounded flows continuity constrains the near-wall vertical velocity fluctuations ($\overline{w^2}$) to scale as $(z/z_i)^{2/3}w_*^2 + \mathrm{O}(u_*^2)$. A similar argument is made by Peltier *et al.* (1996). Hence sufficiently close to the wall, for very small z/z_i, vertical velocity fluctuations scale with u_*^2. In the atmospheric boundary layer, the MO hypothesis leads to

$$\frac{\overline{w^2}}{u_*^2} = \Phi_{w^2}\left(\frac{z}{L}\right), \tag{4.5}$$

where Panofsky *et al.* (1977) empirically observed

$$\Phi_{w^2} = 1.6 + 2.9\left(-\frac{z}{L}\right)^{2/3}. \tag{4.6}$$

Peltier *et al.* used a generic form of the horizontal velocity spectrum for small z/z_i, parameterized from experimental data, in the continuity equation to derive the following expression:

$$\frac{\overline{w^2}}{u_*^2} = 1.6 + 3.7\left(-\frac{z}{L}\right)^{2/3} - 46\left(\frac{z}{z_i}\right)^{4/3}\left(-\frac{z}{L}\right)^{2/3}. \tag{4.7}$$

Because LES provides only the resolved-scale field, it is necessary to estimate the SGS contribution to $\overline{w^2}$, where for a wave-cutoff filter in Fourier space,

$$\overline{w^2} = \overline{w^r w^r} + \overline{w^s w^s}. \tag{4.8}$$

At a level where the simulations resolve the inertial subrange, the SGS contribution $\overline{w^s w^s}$ may be estimated by extending the inertial-subrange spectrum (figure 1) to infinity. Another approach is to estimate $\overline{w^s w^s}$ from the SGS energy e, obtained from a separate prognostic equation (§3.2), by assuming that the unresolved scales are locally isotropic:

$$\overline{w^s w^s} \approx \tfrac{2}{3}\overline{e}. \tag{4.9}$$

We find that at heights where the inertial subrange is well resolved, (4.9) underestimates $\overline{w^s w^s}$ obtained through spectral extension by 4–5%. Moeng (1984) found the difference to be $\approx 9\%$ in 96^3 simulations.

We argue that at heights where the inertial range is well resolved, spectral extension provides the more accurate estimate of $\overline{w^s w^s}$. This is not the case, however, in the under-resolved region ($z < z_r$). Here we find that spectral extension overestimates $\overline{w^s w^s}$, producing unrealistic profiles of $\overline{w^2}$ close to the surface. The estimate from (4.9), however, has the correct trends as $z \to 0$. Thus, to estimate $\overline{w^s w^s}$ consistent with

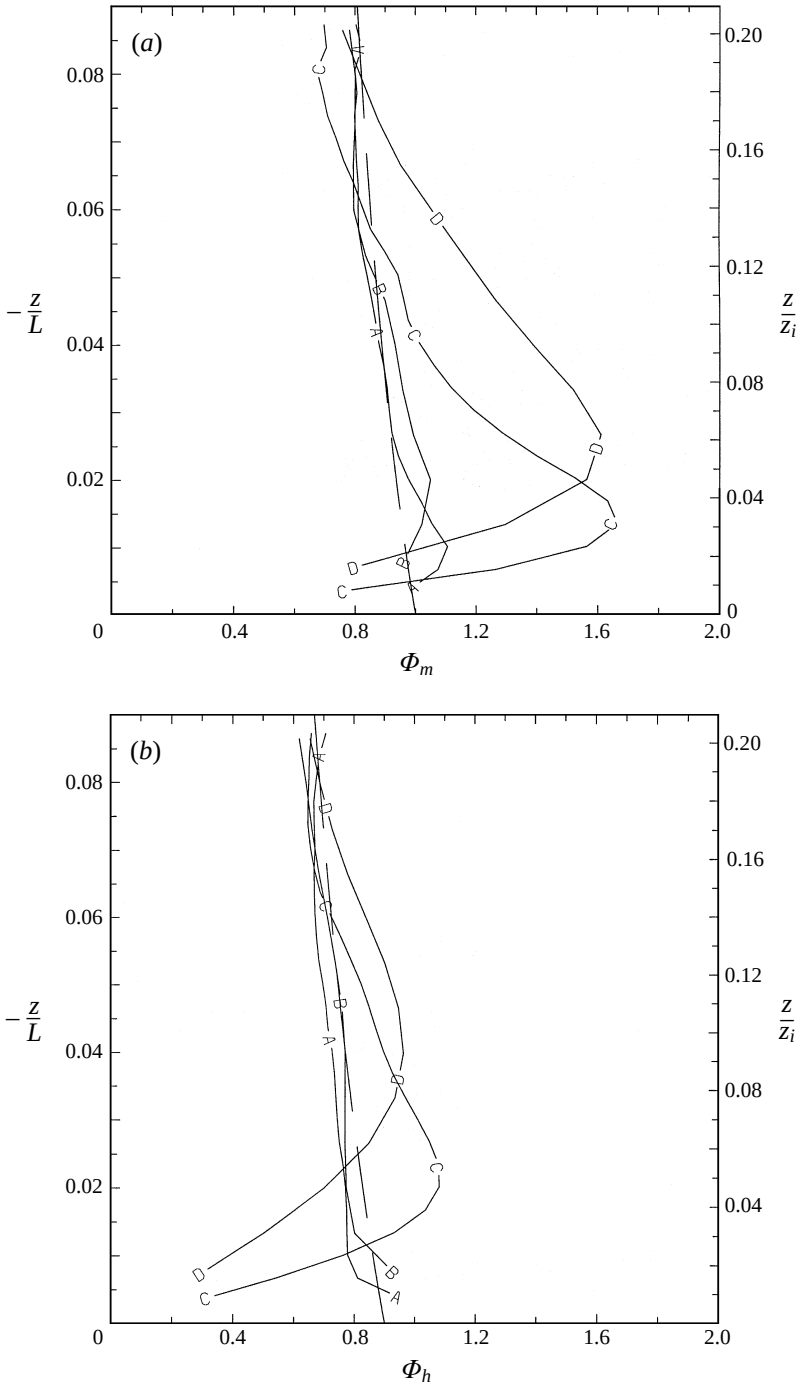

FIGURE 6 (a, b). For caption see facing page.

spectral extension at higher z but with (4.9) as $z \to 0$, we use

$$\overline{w^s w^s} = \alpha \tfrac{2}{3} \overline{e}, \tag{4.10}$$

where α is the ratio of $\overline{w^s w^s}$ obtained from spectral extension to $\frac{2}{3}\overline{e}$ at $z \approx 0.2 z_i$.

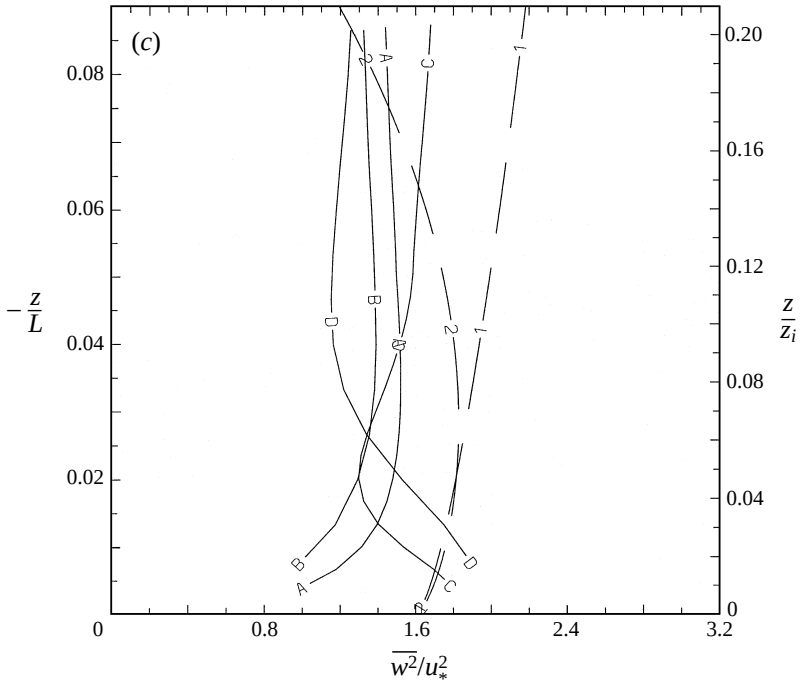

FIGURE 6. MO-normalized (*a*) mean shear (equation (4.1)), (*b*) mean temperature gradient (4.3) and (*c*) vertical velocity variance (4.5), for the $-z_i/L = 0.44$ simulation: curve A, 256^3 embedded mesh using SMM94; curve B, 128^3 using SMM94; curve C, 256^3 embedded mesh using M84; curve D, 128^3 using M84. The dashed line in (*a*) and (*b*) is an empirical fit from Businger *et al.* (1971) and the dashed line 1 in (*c*) is an empirical fit from Panofsky *et al.* (1977). Dashed line 2 in (*c*) is from the spectral model of Peltier *et al.* (1996).

The comparisons for MO-scaled vertical velocity variance are given in figure 6(*c*). Except for a uniform discrepancy in the magnitude, the overall trend predicted by SMM94 SGS parameterization (curves A,B) follow reasonably well both the field observations and the model prediction of Peltier *et al.* at smaller z/z_i where the model applies. Increased resolution significantly improves the SMM94 prediction. The M84 SGS parameterization, on the other hand, produces peculiar near-ground behaviour that moves closer to the ground with increased resolution (curves C,D). The implication is that the M84 parameterization is more sensitive to poor resolution at the first couple of grid points than is the SMM94 parameterization.

Figure 6(*a–c*) suggests that of the four classes of simulations developed for this study, the embedded mesh simulation using the SMM94 parameterization is the most accurate for the compared ensemble-mean statistics. We therefore analyse MO-similar behaviour in more detail using 256^3 embedded mesh LES simulations with the SMM94 parameterization for the three ABL states $-z_i/L = 0.4, 3$ and 8.

5. Statistical structure of the temperature field

In this section we analyse elements of MO similarity observed by the temperature field, focusing on mean potential temperature gradient, temperature variance, the budget of the temperature variance, and the two-dimensional temperature spectrum.

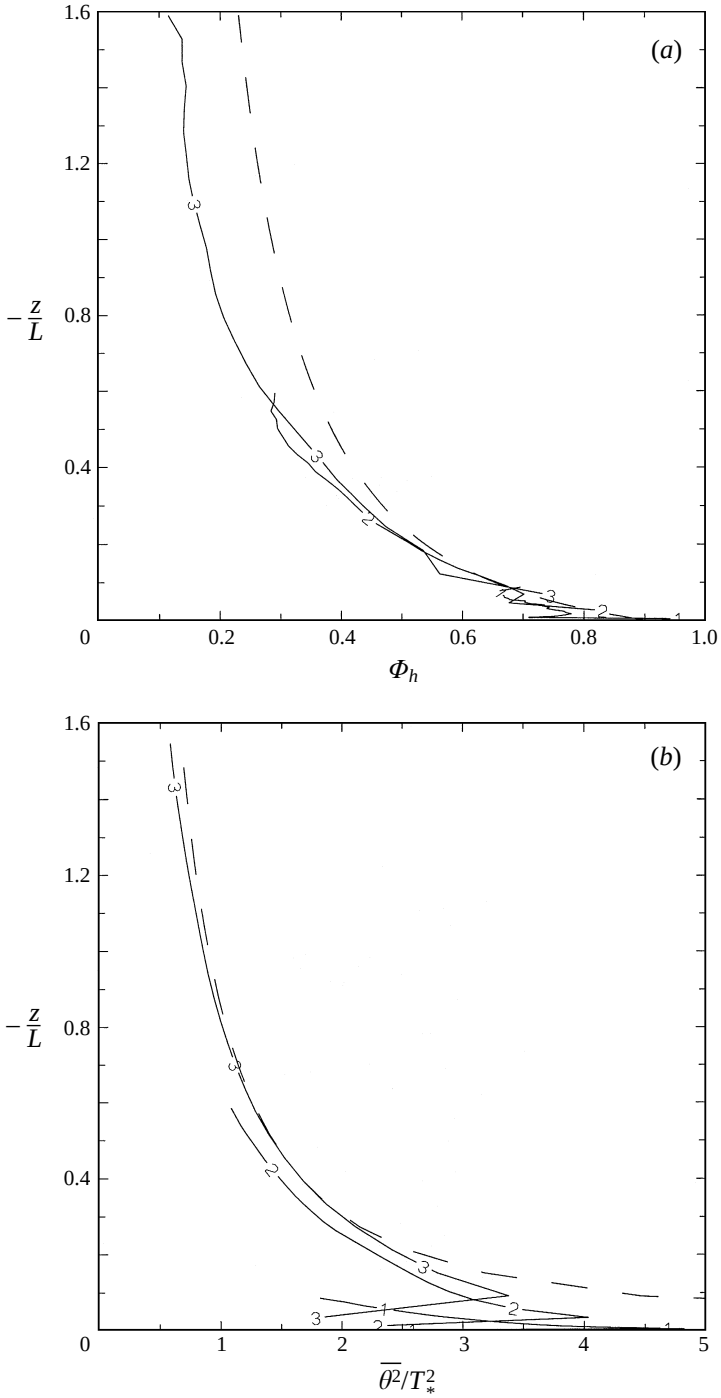

FIGURE 7 (a, b). For caption see facing page.

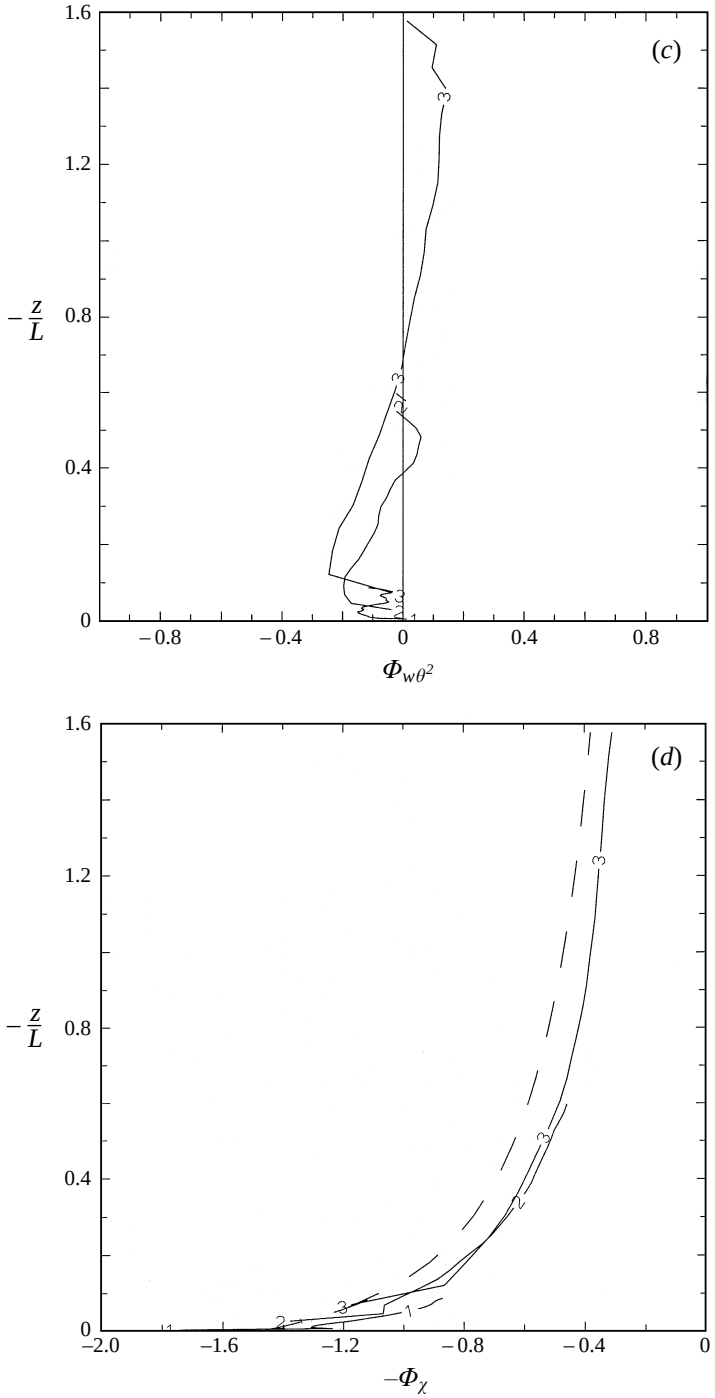

FIGURE 7. MO-normalized (*a*) mean temperature gradient, (*b*) temperature variance, (*c*) turbulent transport of temperature variance, and (*d*) destruction rate of temperature variance, from effective 256^3 embedded mesh simulations: curve 1, $-z_i/L = 0.44$; curve 2, $-z_i/L = 3$; curve 3, $-z_i/L = 8$. Dashed line in (*a*) from Businger *et al.* (1971), in (*b*) from Wyngaard *et al.* (1971) and in (*d*) from Businger *et al.* (1971) (Φ_h, note (5.9)).

5.1. *Mean potential temperature gradient*

The MO prediction of mean potential temperature gradient was discussed in the previous section. The MO-normalized profiles of mean potential temperature gradient (4.3) from the embedded mesh simulations of the three boundary layer states using SMM94 are presented together with the field observations of Businger *et al.* (4.4), with the subsequent modification of the coefficient (see §4), in figure 7(*a*). The profiles from the three atmospheric states collapse well onto a single curve consistent with the MO hypothesis (2.1). The LES results also agree reasonably well with the field observations.

5.2. *Temperature variance*

The MO hypothesis requires

$$\frac{\overline{\theta^2}}{T_*^2} = \Phi_{\theta^2}\left(\frac{z}{L}\right), \tag{5.1}$$

where $T_* = -Q_0/u_*$ is the hypothesized characteristic normalizing scale for temperature fluctuations. It has been observed by Wyngaard *et al.* (1971) and Högström (1990) that even at small $-z/L$ in an otherwise shear-dominated region of the boundary layer, the temperature variance tends to follow 'local free convection' similarity whereby

$$\frac{\overline{\theta^2}}{T_f^2} = A, \tag{5.2}$$

where $T_f = -Q_0/u_f$ and $u_f = (kg/T_0 Q_0 z)^{1/3}$ are the local free-convection temperature and velocity scales (2.2) and A is a constant. Field measurements of Wyngaard *et al.* (1971) indicate that $A \approx 0.9$ and that (5.2) applies when $|z/L| \geqslant 0.5$.

Equation (5.2) can be expressed in MO-similar form as

$$\frac{\overline{\theta^2}}{T_*^2} = A\left(-\frac{z}{L}\right)^{-2/3}. \tag{5.3}$$

Figure 7(*b*) shows the MO-normalized temperature variance profiles as a function of z/L for the three ABL states, and equation (5.3) with $A = 0.9$. The most convective boundary layer ($-z_i/L = 8$) agrees very well with the local-free-convection similarity prediction (5.2). The close-to-neutral boundary layer, on the other hand, has a very different behaviour. Field data for this case are scarce and the data of Högström (1990) show a great deal of scatter at small z/L. The appropriate normalizing scale for the near-neutral case appears to lie between T_* and T_f as suggested by Kader & Yaglom (1990). The $-z_i/L = 3$ boundary layer is similar to $-z_i/L = 8$, but has a slightly lower value for A (≈ 0.82).

It may not be surprising that local-free-convection scaling is observed at small $-z/L$. Consider that under such conditions the near-ground layer contains a mix of shear-induced motions associated with surface shear stress and buoyancy-induced motions associated with surface temperature flux. Shear-induced motions have a characteristic velocity scale u_* while the buoyancy-induced motions have a characteristic velocity scale u_f. From the definition of the MO length scale L (equation (1.1)) it follows that

$$\frac{u_*}{u_f} = \left(-\frac{z}{L}\right)^{-1/3}. \tag{5.4}$$

Although both shear- and buoyancy-driven motions make contribution to near-

ground-layer statistics, (5.4) implies that when $z < L$ the shear-induced motions contribute more to vertical velocity variance than buoyancy-induced motions and u_* is the dominant velocity scale. The opposite is true, however, of temperature variance since the characteristic temperature scales of shear- and buoyancy-induced motions are Q_0/u_* and Q_0/u_f and $T_*/T_f = (-z/L)^{1/3}$. Thus the buoyancy-induced contributions to temperature variance are, on average, larger than the contributions from shear-induced motions when $z < L$ and T_f is the appropriate normalizing scale for temperature variance. When $z > L$ shear production becomes negligible and buoyancy dominates both the temperature and velocity fluctuations.

5.3. *Budget of temperature variance*

Under horizontally homogeneous and quasi-stationary conditions, the budget of temperature variance ($\overline{\theta^2}$) reduces to

$$-2\overline{w\theta}\frac{\partial \Theta}{\partial z} - \frac{\partial \overline{w\theta^2}}{\partial z} - \chi = 0. \tag{5.5}$$

The first term in (5.5) is the gradient production rate, the second term is turbulent transport of temperature variance and χ is the molecular destruction rate.

For horizontal homogeneity and stationarity the fluxes of temperature and momentum vary linearly from the surface to the 'capping inversion' (see Wyngaard 1992). Since the flux at $z = 0$ is fixed by Q_0, $\overline{w\theta} \approx Q_0$ in the near-ground layer and the MO-normalized production rate is given by

$$-2\frac{kz}{u_* T_*^2} Q_0 \frac{\partial \Theta}{\partial z} = 2\frac{kz}{T_*}\frac{\partial \Theta}{\partial z} = 2\Phi_h\left(\frac{z}{L}\right). \tag{5.6}$$

As discussed in §5.1, Φ_h from the simulations agree well with field measurements (figure 7*a*).

The MO-normalized turbulent transport term is given by

$$-\frac{kz}{u_* T_*^2}\frac{\partial \overline{w\theta^2}}{\partial z} = \Phi_{w\theta^2}\left(\frac{z}{L}\right). \tag{5.7}$$

Because LES provides only the resolved-scale fields, we have no choice but to approximate (5.7) with $\partial \overline{w^r \theta^{r2}}/\partial z$, the transport of resolved temperature variance by resolved-scale motions. Figure 7(*c*) shows the profiles of resolved-scaled MO-normalized flux from our three simulations.

Wyngaard & Coté (1971) found that the transport term was an order of magnitude smaller than the production term. Their data had a great deal of scatter and did not show a definite trend with z/L, but did indicate a change of sign from a loss at smaller z/L to a gain at large z/L. The range of $\Phi_{w\theta^2}$ observed in figure 7(*c*) agrees well with the range observed by Wyngaard & Coté. Furthermore the most convective case shows a change in sign from smaller to larger z/L consistent with the field measurements.

Because the turbulent transport term is an order of magnitude smaller than the production term, there is a near balance between production and destruction. Thus, the MO-normalized destruction rate of scalar variance,

$$\Phi_\chi\left(\frac{z}{L}\right) = \frac{kz}{u_* T_*^2}\chi, \tag{5.8}$$

is approximately equal to the MO-normalized temperature gradient:

$$\Phi_\chi \approx 2\Phi_h. \tag{5.9}$$

In LES with the filter cutoff in the inertial range the molecular destruction rate of scalar variance balances the spectral flux of scalar variance from resolved to unresolved scales. Thus

$$\chi = -2\overline{Q_i \frac{\partial \Theta^r}{\partial x_i}}. \tag{5.10}$$

Figure 7(*d*) shows the MO-normalized destruction rate obtained for the three cases. The profiles compare well with $2\Phi_h$ in figure 7(*a*) and collapse onto a single curve. We conclude that the rates of production and destruction of scalar variance are governed by MO scales and follow the MO hypothesis.

5.4. *Temperature spectra*

For a horizontally homogeneous boundary layer, a two-dimensional Fourier expansion is appropriate in horizontal directions:

$$\theta(x, y, z) = \int \hat{\theta}(k_1, k_2, z) \mathrm{e}^{\mathrm{i}(k_1 x + k_2 y)}\, \mathrm{d}k_1\, \mathrm{d}k_2, \tag{5.11}$$

where $\hat{\theta}(\boldsymbol{\kappa}, z)$ is the Fourier coefficient for the horizontal wavevector $\boldsymbol{\kappa} = (k_1, k_2)$. The two-dimensional temperature spectrum is

$$E_\theta^{(2)}(\kappa, z) = \int_0^{2\pi} \psi^{(2)}(\boldsymbol{\kappa}, z)\kappa\, \mathrm{d}\alpha, \tag{5.12}$$

where $\psi^{(2)}(\boldsymbol{\kappa}, z) = \overline{\hat{\theta}(\boldsymbol{\kappa}, z)\hat{\theta}^*(\boldsymbol{\kappa}, z)}$, $\kappa^2 = k_1^2 + k_2^2$ and $\boldsymbol{\kappa} = (\kappa\cos\alpha, \kappa\sin\alpha)$.

The Kolmogorov arguments extended for the two-dimensional temperature spectrum in the inertial subrange imply

$$E_\theta^{(2)}(\kappa, z) = \beta_2 \chi \epsilon^{-1/3} \kappa^{-5/3}, \tag{5.13}$$

where $\beta_2 = \beta_1/0.71$ (see Peltier *et al.* 1995) is a universal constant for the two-dimensional spectrum and ϵ and χ are functions of z (χ was defined in §5.3). Gal-Chen & Wyngaard (1982) show that the one-dimensional spectrum of a filtered field can, in principle, depart from $\kappa^{-5/3}$ in the inertial range depending on the choice of filter. Moeng & Wyngaard (1988) show that a finite number of modes in the simulation can cause further deviations in the inertial-subrange prediction of the one-dimensional spectrum. We extended the analysis of Gal-Chen & Wyngaard and Moeng & Wyngaard to the two-dimensional spectrum obtained from the resolved LES fields, where the central-differencing approximation in z was treated as a top-hat filtering. The maximum deviation, however, was only $\approx 2\%$ at the highest κ wavenumber.

The MO-normalized two-dimensional spectrum (5.13) can be expressed as

$$\frac{\kappa E_\theta^{(2)}}{T_*^2} = \frac{\beta_2}{k^{2/3}} \Phi_\chi \Phi_\epsilon^{-1/3} (\kappa z)^{-2/3}, \tag{5.14}$$

where k is the von Kármán constant, Φ_χ and Φ_ϵ are the MO-normalized destruction rate of temperature variance (equation (5.8)) and dissipation rate (equation (6.4)), respectively, each a function only of z/L under the MO hypothesis. Equation (5.14)

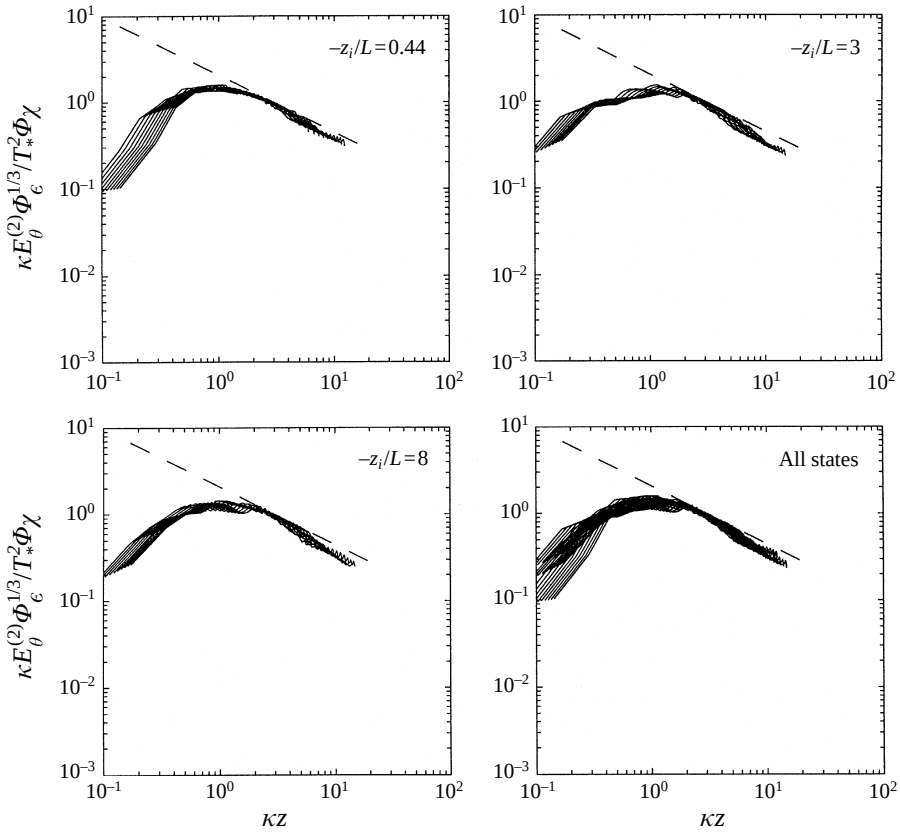

FIGURE 8. MO-normalized two-dimensional temperature spectra from effective 256^3 embedded mesh simulations. Different solid lines are from 10 z levels ($0.05 \leqslant z/z_i \leqslant 0.12$). Dashed line is the right-hand side of (5.15).

can be rewritten

$$\frac{\kappa E_\theta^{(2)}\Phi_\epsilon^{1/3}}{T_*^2\Phi_\chi} = \frac{\beta_2}{k^{2/3}}(\kappa z)^{-2/3}. \tag{5.15}$$

Figure 8 shows the left-hand side of (5.15) as a function of the non-dimensional wavenumber κz at different heights in the near-ground layer with $\beta_2 = 0.56$. All curves collapse well in the inertial subrange as predicted by (5.15) under the MO hypothesis suggesting that the inertial-range temperature variance is MO-similar.

The collapsed non-dimensional spectrum agrees well with the inertial-subrange predictions except close to the filter cutoff where the spectrum is attenuated despite corrections for filtering and finite mode approximation. This deviation is likely a consequence of the SGS parameterization, which has its strongest effects near the filter cutoff.

6. Statistical structure of the velocity field

In this section we analyse the statistical structure of mean shear, velocity variance, the budget of turbulent kinetic energy and two-dimensional velocity spectra in the context of MO-similarity, extending the discussion in §4.

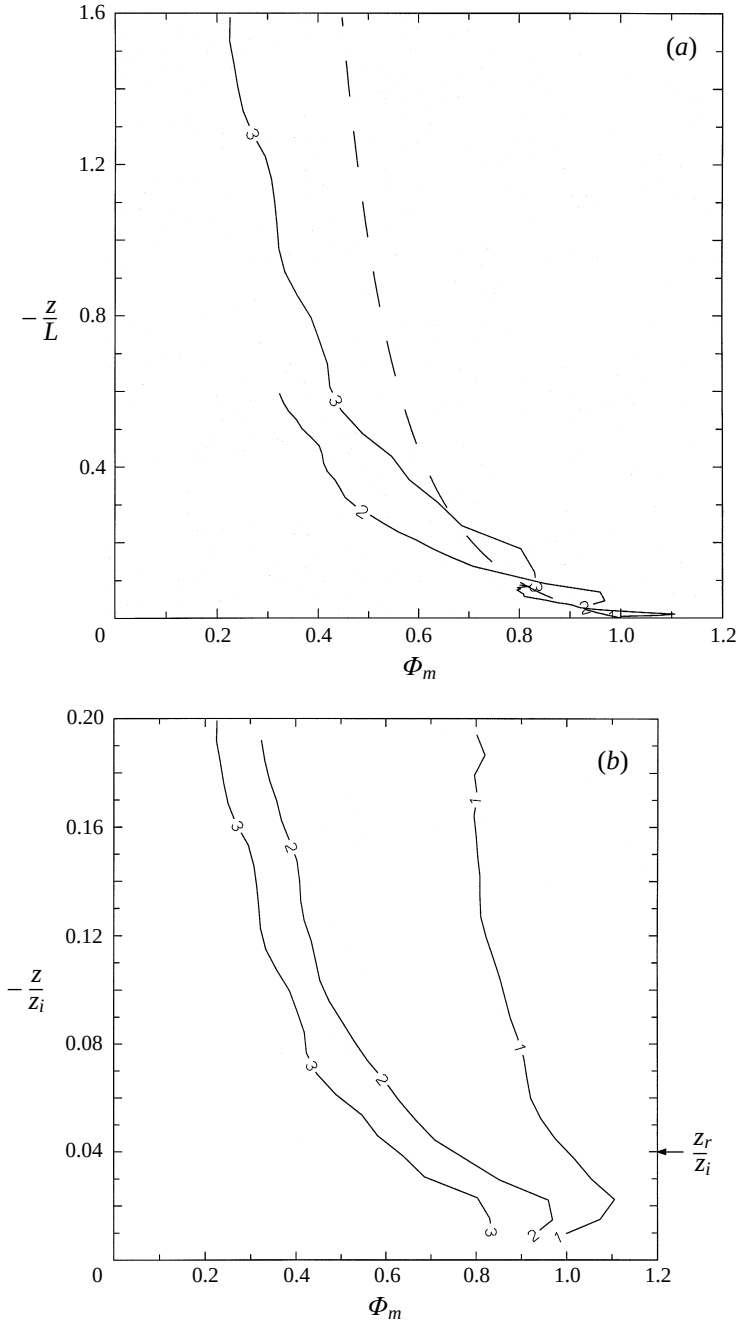

FIGURE 9. MO-normalized mean shear from effective 256^3 embedded mesh simulations: curve 1, $-z_i/L = 0.44$; curve 2, $-z_i/L = 3$; curve 3, $-z_i/L = 8$. Dashed line from Businger *et al.* (1971).

6.1. *Mean shear*

Mean shear under the MO hypothesis was given in equation (4.1):

$$\frac{kz}{u_*}\frac{\partial U}{\partial z} = \Phi_m\left(\frac{z}{L}\right). \tag{6.1}$$

Figure 9(*a*) shows the MO-normalized mean shear profiles from the three 256^3 embedded mesh simulations with the SMM94 SGS parameterization. The three profiles do not collapse well under MO scaling suggesting either a potential influence from mixed-layer scales or a lack of resolution in the simulations at sufficiently small z/z_i to observe a collapse in the range $-z_i/L = 0.44$–8.

The simulations indicate that, as discussed in §2, the mixed-layer scales have an indirect influence on the near-ground layer whereby forms (2.3), (2.4) or (2.5) are appropriate. Figure 9(*a*) suggests that the MO parameters are appropriate normalizing scales since $\Phi_m \sim O(1)$ for all three atmospheric states, but that a systematic dependence on z_i/L may exist. Because the embedded mesh covers the same z/z_i range in all three simulations, form (2.5), plotted in figure 9(*b*), is most likely to show systematic variations with $-z_i/L$. We observe from figure 9(*b*) that $-z_i/L = 3$ and $-z_i/L = 8$ have apparently self-similar profiles different from the $-z_i/L = 0.44$ state. In §4 we observed that the MO-scaled mean shear for the near-neutral case agreed with field observations up to $z/z_i \approx 0.15$. It appears, then, that the two more convective cases have a structure different from the near-neutral case and that even relatively low levels of buoyancy forces introduce an indirect influence from the mixed-layer scales on the near-ground layer.

There is no experimental evidence indicating the form observed in figure 9(*b*). It is possible, as mentioned in §4, that the under-resolved region in LES influences the overall predictions of the near-ground layer. Nevertheless, the form suggested in figure 9(*b*) is interesting and needs further verification by field measurements of resolved-scale variables with proper documentation of boundary layer depth.

6.2. *Vertical velocity variance*

The MO hypothesis predicts that

$$\frac{\overline{w^2}}{u_*^2} = \Phi_{w^2}\left(\frac{z}{L}\right). \tag{6.2}$$

The field observations of Panofsky *et al.* (1977) and theoretical predictions of Peltier *et al.* (1995) were discussed in §4 (equations (4.6) and (4.7)). Figure 10(*a*) shows the MO-normalized vertical velocity variance obtained from the three 256^3 embedded mesh simulations. Like mean shear, the three curves do not collapse under MO scaling. Nevertheless, the vertical velocity variances from all three simulations do appear to scale on u_*^2 near the ground, suggesting again the possibility of an indirect influence from the mixed-layer eddies.

From (2.5), figure 10(*b*) shows the MO-normalized vertical velocity variance plotted as a function of z/z_i. The three curves do not collapse or show any obvious self-similar behaviour, indicating a complex functional dependence on both z/z_i and z_i/L. However, it is interesting to compare the near-collapse of curves 1 and 2 ($-z_i/L = 0.44$ and 3) in figure 10(*b*) with the apparent self-similar form of curves 2 and 3 ($-z_i/L = 3$ and 8) in figure 9(*b*), suggesting that $-z_i/L = 3$ is, in some sense, transitional between the near-neutral ($-z_i/L = 0.44$) and the moderately convective ($-z_i/L = 8$) boundary layer states.

It is also interesting to observe that the three MO-normalized $\overline{w^2}$ curves in figure 10(*b*) appear to collapse to a universal form very close to the ground, at the first grid point. This apparent collapse must be viewed with caution, however, since this occurs at heights where the large-eddy scales are not fully resolved ($z < z_r$), and where the resolved-scale statistics, which include estimates for the SGS contributions, are highly questionable.

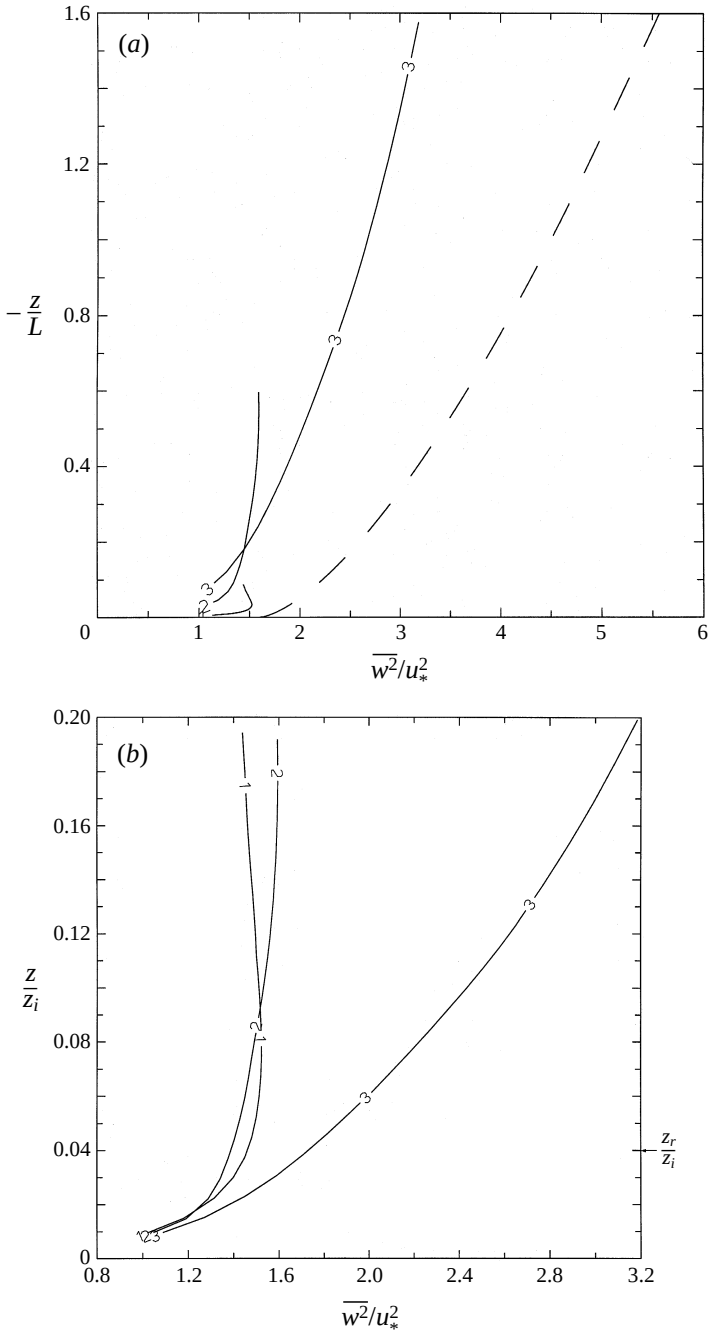

FIGURE 10. MO-normalized vertical velocity variance from effective 256^3 embedded mesh simulations: curve 1, $-z_i/L = 0.44$; curve 2, $-z_i/L = 3$; curve 3, $-z_i/L = 8$. The dashed line is an empirical fit from Panofsky *et al.* (1977).

6.3. *Horizontal velocity variance*

Measurements of Panofsky *et al.* (1977) and numerical simulations of Deardorff (1972) show that the horizontal fluctuations within the near-ground layer of a convective

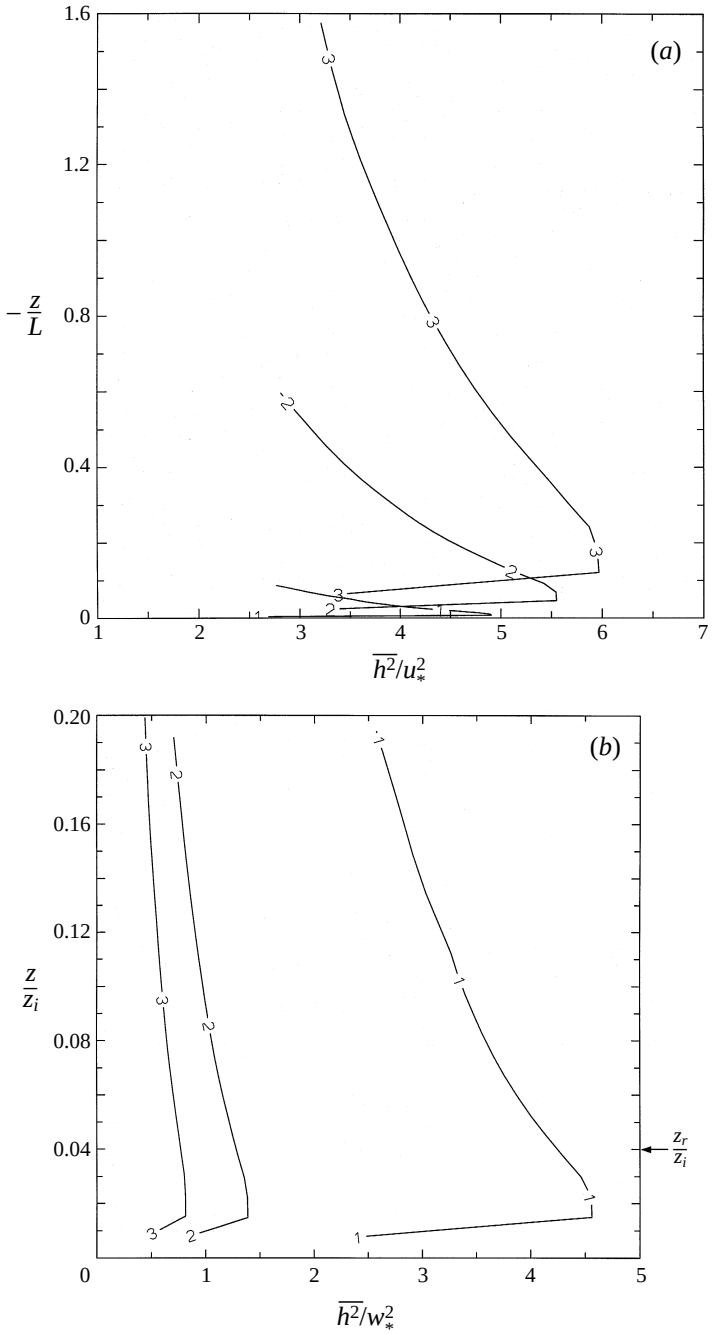

FIGURE 11. (*a*) MO-normalized and (*b*) w_*^2-normalized horizontal velocity variance from effective 256^3 embedded mesh simulations; curve 1: $-z_i/L = 0.44$; curve 2: $-z_i/L = 3$; curve 3: $-z_i/L = 8$.

boundary layer are directly influenced by the mixed-layer eddies and that these fluctuations scale with the mixed-layer length and velocity scales z_i, w_*. Figure 11(*a*) shows the MO-scaled horizontal velocity variances ($\overline{h^2} = 1/2[\overline{u^2} + \overline{v^2}]$) for the three simulated ABL states. As expected, u_* is not an appropriate normalizing scale and the

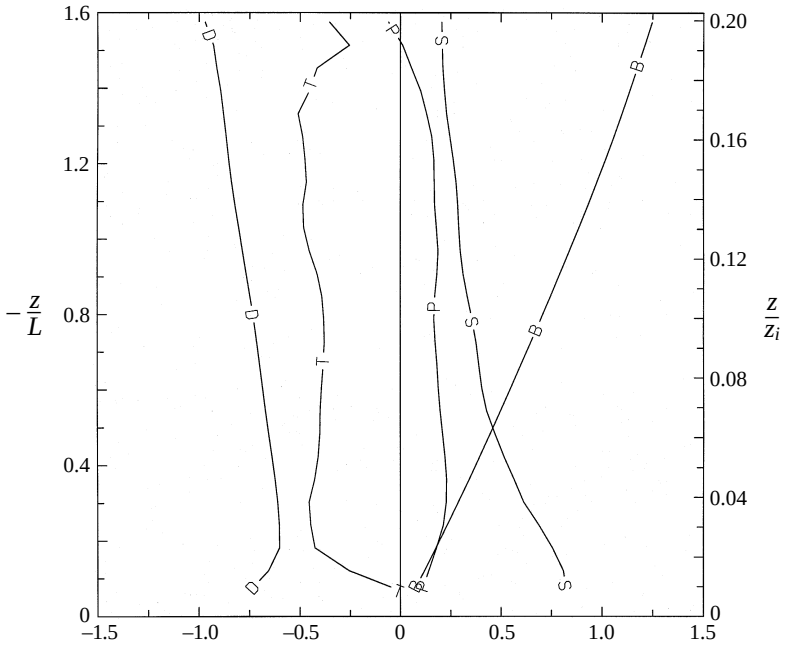

FIGURE 12. MO-normalized turbulent kinetic energy budget from effective 256^3 embedded mesh simulation with $-z_i/L = 8$: curve S, shear production; curve B, buoyant production; curve T: turbulent transport; curve P, pressure transport; and curve D, dissipation.

profiles do not collapse. Figure 11(*b*) shows the horizontal variances normalized by w_*^2 plotted against z/z_i. The mixed-layer velocity scale w_* is apparently the appropriate normalizing scale and, like mean horizontal velocity (figure 9*b*), the near-neutral case has a very different behaviour than the moderately convective $-z_i/L = 3$ and 8 states. The more convective case $-z_i/L = 8$ is consistent with the observations of Panofsky *et al.* for highly convective boundary layers, who observed $\overline{h^2}/w_*^2 \approx 0.6$ at large $-z_i/L$.

6.4. *Budget of turbulent kinetic energy*

Under horizontally homogeneous and quasi-steady conditions, the budget of turbulent kinetic energy (TKE) $\overline{u_i u_i}/2$ reduces to

$$-\overline{uw}\frac{\partial U}{\partial z} + \frac{g}{T_0}\overline{w\theta} - \frac{1}{2}\frac{\partial \overline{wq^2}}{\partial z} - \frac{1}{\rho_0}\frac{\partial \overline{wp}}{\partial z} - \epsilon = 0, \tag{6.3}$$

where $q^2 = u_i u_i$. The terms in (6.3) are, respectively, shear production, buoyant production, turbulent transport, pressure transport and the dissipation rate. According to the MO hypothesis, these individual terms non-dimensionalized by kz/u_*^3 should be functions only of z/L.

Figure 12 shows the overall TKE budget non-dimensionalized by kz/u_*^3 within the near-ground layer for $-z_i/L = 8$. Qualitatively, the budget agrees with field observations (see Wyngaard 1992). Pressure transport is a gain while turbulent transport is a loss. Shear production peaks at the ground and buoyant production becomes dominant at $z \approx 0.5L$.

We analysed individual terms in (6.3) for MO scaling. Under horizontally homogeneous, quasi-steady and barotropic states the turbulent fluxes ($\overline{uw}, \overline{w\theta}$) vary linearly from their respective surface values to the entrainment flux at the capping inversion (Wyngaard 1992). Taking the traditional approach in which the momentum and temperature flux are given their surface values within the near-ground layer (see also §5.3), the terms in (6.3) become under MO scaling

$$\left.\begin{aligned} -\frac{kz}{u_*^3}\overline{uw}\frac{\partial U}{\partial z} \approx \frac{kz}{u_*}\frac{\partial U}{\partial z} = \Phi_m\left(\frac{z}{L}\right), \quad \frac{kz}{u_*^3}\frac{g}{T_0}\overline{w\theta} \approx \frac{kz}{u_*^3}\frac{g}{T_0}Q_0 = -\frac{z}{L}, \\ -\frac{kz}{u_*^3}\frac{1}{2}\frac{\overline{wq^2}}{\partial z} = \Phi_{wq^2}\left(\frac{z}{L}\right), \quad -\frac{kz}{u_*^3}\frac{1}{\rho_0}\frac{\partial \overline{wp}}{\partial z} = \Phi_{wp}\left(\frac{z}{L}\right), \quad \frac{kz}{u_*^3}\epsilon = \Phi_\epsilon\left(\frac{z}{L}\right). \end{aligned}\right\} \tag{6.4}$$

Figure 13(*a*) shows MO-scaled turbulent transport from our simulations, where the transport term is approximated as

$$-\frac{1}{2}\frac{\partial \overline{wq^2}}{\partial z} \approx -\frac{1}{2}\frac{\partial \overline{w^r u_i^r u_i^r}}{\partial z} - \frac{\partial \overline{w^r e}}{\partial z}, \tag{6.5}$$

the transport of resolved- plus subgrid-scale kinetic energy by resolved-scale turbulence fluctuations. The resolved–subgrid and subgrid–subgrid interaction terms which could not be included in (6.5) are only important near the ground where the large scales are not well resolved. Note in figure 13(*a*) that the three profiles do not collapse under MO scaling. Indeed, turbulent transport is roughly constant in the near-ground layer with a value that increases with increasing $-z_i/L$. Whereas transport is negligible under near-neutral conditions, it becomes of $O(1)$ at higher $-z_i/L$. The measurements of Wyngaard & Coté (1971) at small z/z_i suggest a balance between transport and buoyant production. However, there was a great deal of scatter in their data.

Figure 13(*b*) shows the MO-scaled pressure transport approximated using resolved variables:

$$\frac{1}{\rho_0}\frac{\partial \overline{wp}}{\partial z} \approx \frac{1}{\rho_0}\frac{\partial \overline{w^r p^r}}{\partial z}. \tag{6.6}$$

Equation (6.6) is a reasonable approximation when $z > z_r$. Again we observe no evidence of a collapse under MO scaling with pressure transport being fairly constant in the near-ground layer. Wyngaard & Coté (1971) could only estimate this term from the imbalance in the TKE budget. Because they found turbulent transport and buoyant production to nearly balance, they estimate MO-scaled pressure transport as

$$\Phi_{wp}\left(\frac{z}{L}\right) = -\Phi_m\left(\frac{z}{L}\right) + \Phi_\epsilon\left(\frac{z}{L}\right). \tag{6.7}$$

Equation (6.7) gives much higher values of Φ_{wp} at higher $-z_i/L$ than do the simulations (figure 13*b*). However, there is a great deal of uncertainty in the field estimates. There are some direct measurements of the pressure transport term (see Oncley *et al.* 1995). However, the data are very limited and have a great deal of scatter.

Figure 13(*c*) shows the MO-scaled dissipation rate for the three boundary layer states, where dissipation rate balances the flux of energy from resolved to subgrid scales:

$$\epsilon = -\overline{\tau_{ij}\frac{\partial u_i^r}{\partial x_j}}. \tag{6.8}$$

Note from figure 13(*c*) that the dissipation rate scales well with kz/u_*^3 and that

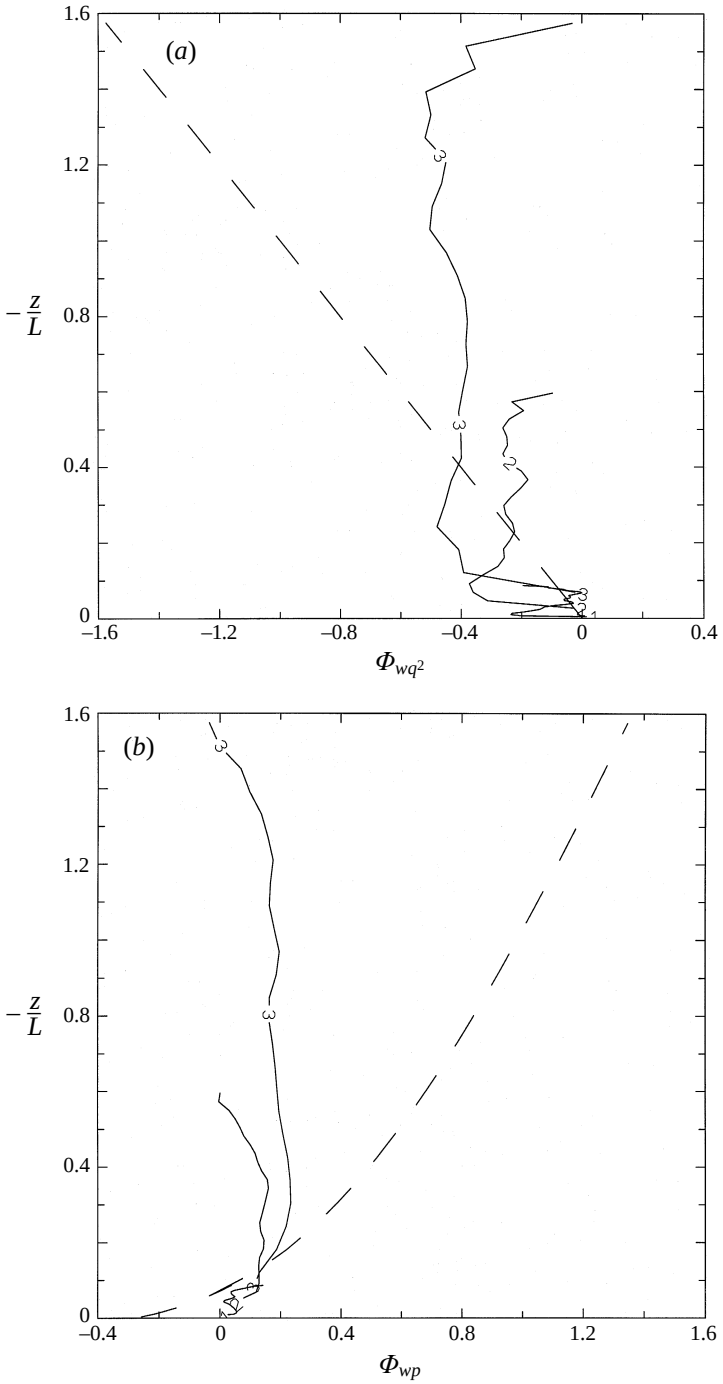

FIGURE 13 (a, b). For caption see facing page.

there is some indication of a collapse when $z/z_i < 0.1$. Like Högström (1990) the simulations predict a minimum MO-scaled dissipation rate away from the ground (dashed curve A). The measurements of Wyngaard & Coté (1971), on the other hand, have a minimum at the ground with an increasing magnitude away from the ground

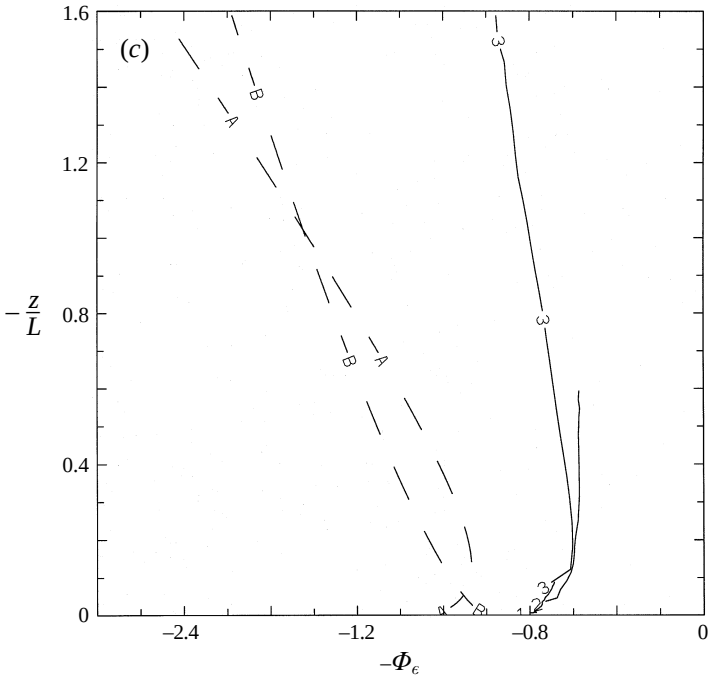

FIGURE 13. MO-normalized (*a*) turbulent transport, (*b*) pressure transport and (*c*) dissipation rate, of TKE from 256^3 embedded mesh simulations: curve 1, $-z_i/L = 0.44$; curve 2, $-z_i/L = 3$; curve 3, $-z_i/L = 8$. Dashed line in (*a*), (*b*) and line B in (*c*) from Wyngaard & Coté (1971); dashed line A in (*c*) from Högström (1990).

(dashed curve B). In its trends the agreement between field measurements and the LES predictions is quite reasonable.

6.5. *Velocity spectra*

The two-dimensional Fourier representation of the velocity field is given by

$$u_i(x, y, z) = \int \hat{u}_i(k_1, k_2, z) \mathrm{e}^{\mathrm{i}(k_1 x + k_2 y)} \, \mathrm{d}k_1 \mathrm{d}k_2, \tag{6.9}$$

where $\hat{u}_i(\boldsymbol{\kappa}, z)$ is the Fourier coefficient for horizontal wavevector $\boldsymbol{\kappa} = (k_1, k_2)$ at height z. Following Peltier *et al.* (1995), the two-dimensional horizontal energy spectrum is defined

$$E_h^{(2)}(\kappa, z) = \frac{1}{2} \int_0^{2\pi} (\phi_{11}^{(2)} + \phi_{22}^{(2)}) \kappa \, \mathrm{d}\alpha, \tag{6.10}$$

where $\phi_{ij}^{(2)}(\boldsymbol{\kappa}, z)\mathrm{d}k_1 \mathrm{d}k_2 = \overline{\hat{u}_i(\boldsymbol{\kappa}, z)\, \hat{u}_j(\boldsymbol{\kappa}, z)}$ and $\int_0^\infty E_h^{(2)}(\kappa, z)\, \mathrm{d}\kappa = \frac{1}{2}(\overline{u^2} + \overline{v^2})$. Similarly, the two-dimensional vertical velocity spectrum is given by

$$E_v^{(2)}(\kappa, z) = \int_0^{2\pi} \phi_{33}^{(2)} \kappa \, \mathrm{d}\alpha, \tag{6.11}$$

and $\int_0^\infty E_v^{(2)}(\kappa, z)\, \mathrm{d}\kappa = \overline{w^2}$.

In the inertial range the Kolmogorov arguments yield

$$E_{h,v}^{(2)}(\kappa, z) = \sigma_{h,v} \epsilon^{2/3} \kappa^{-5/3} \tag{6.12}$$

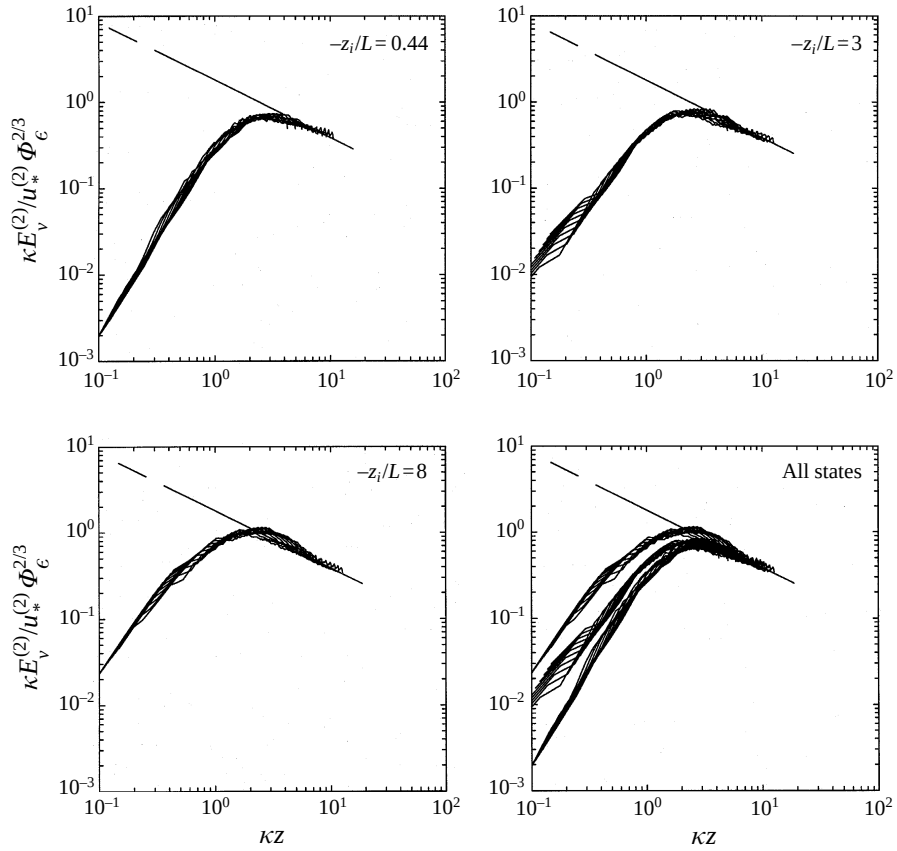

FIGURE 14. MO-normalized two-dimensional vertical velocity spectra from effective 256^3 embedded mesh simulations. Different solid lines are from 10 z levels ($0.05 \leqslant z/z_i \leqslant 0.12$). Dashed line is the right-hand side of (6.13) for w.

where $\sigma_h = \frac{7}{6}\alpha_1/0.71, \sigma_v = \frac{8}{7}\sigma_h$ (see Peltier *et al.* 1995) are the universal constants for two-dimensional velocity spectra and $\alpha_1 = 0.5$.

In §5.4 it was mentioned that the energy spectrum of a filtered field with a finite number of modes can deviate from its inertial-range prediction. A similar analysis was done for the velocity field and the deviations were found to be negligibly small ($\approx 2\%$ at the highest wavenumber).

Under MO scaling the two-dimensional velocity spectra in the inertial range are

$$\frac{\kappa E_{h,v}^{(2)}}{u_*^2 \Phi_\epsilon^{2/3}} = \frac{\sigma_{h,v}}{k^{2/3}}(\kappa z)^{-2/3}. \tag{6.13}$$

Figure 14 shows MO-scaled vertical velocity spectra at different heights within the near-ground layer. For separate atmospheric states the spectra over the range of simulated κz agree well with inertial-range predictions. However, whereas the spectra for the three atmospheric states collapse well in the inertial range, systematic deviations are observed at the integral scales consistent with the discussion in §6.2 (figure 10*a*). It is interesting to find that although the large-scale vertical fluctuations are sensitive to indirect external influences, the inertial-scale motions are not.

Even more interesting is that the inertial-range horizontal velocity fluctuations

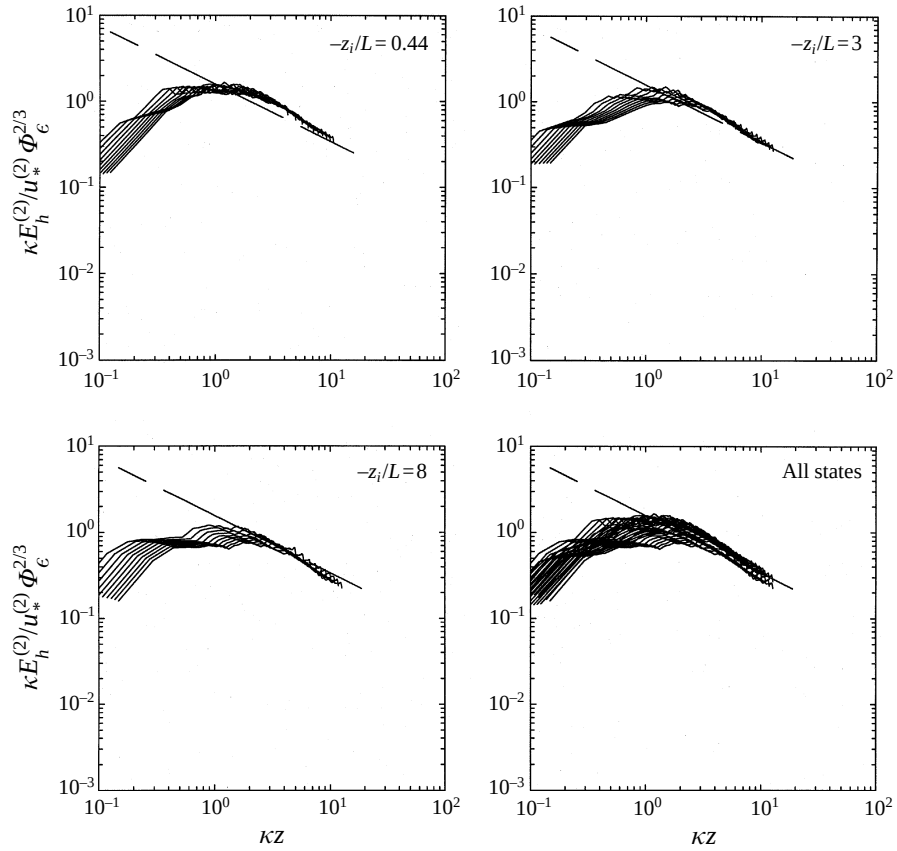

FIGURE 15. MO-normalized two-dimensional horizontal velocity spectra from effective 256^3 embedded mesh simulations. Different solid lines are from 10 z levels ($0.05 \leqslant z/z_i \leqslant 0.12$). Dashed line is the right-hand side of (6.13) for h.

appear to be MO-similar even as the large-scale sweeping motions are dominated by mixed-layer motions. This is shown by the MO-scaled horizontal velocity spectra in figure 15. The scaled spectra collapse only in the inertial range, and the collapsed form agrees well with equation (6.13). We observed in §6.3 that both w_* and z_i are important scaling parameters for horizontal variance (figure 11*b*). Hunt & Graham (1978) and Peltier *et al.* (1996) have shown that continuity constrains the influence of outer-layer eddies to be more pronounced on horizontal fluctuations than on the vertical fluctuations and hence the horizontal fluctuations scale on w_* and z_i. At high wavenumbers, though, local isotropy suggests that the horizontal and vertical velocity fluctuations are of the same order. Thus, we might anticipate local near-ground scaling in the inertial range of horizontal fluctuations even with mixed-layer scaling at the integral scales.

7. Conclusions

We carried out a detailed analysis of the Monin–Obukhov similarity from high-resolution large-eddy simulation data. Although LES provides complete time-dependent three-dimensional information of the large-scale fields, MO-similarity is a near-ground phenomenon and there are numerical difficulties in simulating this region

that hinder a detailed analysis. Recent studies to improve LES predictions of near-ground-layer statistics through modified subgrid-scale parameterization addressed mean shear and mean potential temperature gradient primarily in the near-neutral state. Here we analyse the extent to which LES predictions of other relevant statistics observe MO-similarity and we analyse the relative roles of grid resolution and SGS parameterization on LES predictions of MO-similarity.

LES always fails to resolve the large-scale motions at the first few grid points. To reduce the under-resolved region and improve LES predictions through increased near-ground-layer resolution, we employ an embedded mesh technique with one-way communication, wherein the coarse mesh provides the upper boundary conditions for the fine mesh and there is no feedback from the fine to the coarse mesh. This strategy was validated by comparing an effective 192^3 embedded mesh simulation within a coarser 128^3 mesh with a complete 192^3 simulation. Both the statistical structure and the local three-dimensional structure compared very well.

We compared effects of grid resolution and SGS parameterization on LES predictions of mean shear and temperature gradient and vertical velocity variance for a near-neutral state ($-z_i/L = 0.44$). In particular, the SGS parameterizations of Moeng (1984) and Sullivan *et al.* (1994) were compared on a 128^3 mesh and an effective 256^3 embedded mesh. The Sullivan *et al.* SGS parameterization was significantly better at the same grid resolution and increased resolution moved remaining discrepancies closer to the ground.

We analysed in detail MO-scaled statistics from three effective 256^3 embedded mesh simulations using the Sullivan *et al.* SGS parameterization for the ABL states $-z_i/L = 0.44$, 3 and 8. To the extent possible the LES predictions were compared with field observations.

The restricted ability of LES to resolve very close to the ground raises some fundamental differences between LES and field data. Most importantly, it is not clear over what non-dimensional height z_{MO}/z_i MO-similarity characterizes the statistical structure of a particular variable, or the variation in z_{MO}/z_i with the stability state of the boundary layer. In LES the lowest height z_r above which the large-scale motions are well resolved is restricted by computational resources. We estimate that our 256^3 embedded mesh simulations are well resolved above $z_r/z_i \approx 0.04$. Field measurements of near-ground-layer statistics, on the other hand, are generally collected at lower levels and do not generally quote z_i, making direct comparisons with LES difficult.

Our LES results indicate that, overall, the temperature field is MO-similar and agrees well with field observations in a region near the ground. The MO-normalized profiles of mean shear, temperature variance and terms within the budget of temperature variance collapse when plotted against z/L. Consistent with field observations, we find that the temperature variance satisfies free-convection scaling, even at small z/L. Also consistent with field data, the turbulent transport term is an order of magnitude smaller than the other terms in the temperature variance budget. The inertial-range form of the temperature spectra, on the other hand, did not follow free-convection scaling, but collapsed well under MO scaling. We are left with the important conclusion that different scalings apply in different spectral regions.

The velocity field, on the other hand, showed some distinct departures from MO-similarity. The MO-normalized mean shear, for example, for the near-neutral case appears to agree with the observed form of Φ_m up to $z/z_i \approx 0.15$. However, the three profiles do not collapse under MO scaling and the two moderately buoyant states ($-z_i/L = 3, 8$) display a distinctly different behaviour from the near-neutral state. It appears that even though mean shear scales on MO parameters, the MO-normalized

mean shear has a functional dependence which includes indirect effects from the outer mixed-layer motions:

$$\frac{\kappa z}{u_*}\frac{\partial U}{\partial z} = \Phi'_m\left(\frac{z}{L}, \frac{z}{z_i}\right). \tag{7.1}$$

The integral-scale velocity field statistics, in general, follow equation (2.3).

We concluded from the analysis of the temperature spectra that different ranges of scales scale differently. It is interesting that this conclusion appears to be a general one. We find that both the vertical and horizontal velocity spectra are MO-similar in the inertial scales while departing significantly from MO similarity at the integral scales. Whereas the large vertical velocity scales, like the vertical velocity variance, display a clear influence from the outer length scale z_i, the inertial-range motions collapse under MO scaling among the three atmospheric states analysed. More surprising is a similar collapse under MO scaling observed in the horizontal velocity spectrum, while the integral-scale motions scale entirely on mixed-layer velocity and length scales. Small-scale motions appear to statistically organize around local MO scales independent of outer scale influences at the large scales.

It is clear, from this study, that the statistical organization of the atmospheric near-ground layer is incomplete. Further advances in both experimental and simulation data collection methods are needed to understand the more complex scalings suggested by this work.

This work was supported under a grant from the Army Research Office, grant number DAAL03-92-G-0117, monitored by Walter D. Bach, Jr. We are grateful to John C. Wyngaard for many useful discussions and for review of the manuscript. Peter P. Sullivan of NCAR was very helpful in developing the 'embedded mesh' algorithm, and we thank Chin-Hoh Moeng for the use of her LES code.

REFERENCES

Banta, R. M. 1985 Late-morning jump in TKE in the mixed layer over a mountain basin. *J. Atmos. Sci.* **42**, 407–411.

Businger, J. A., Wyngaard, J. C., Izumi, Y. & Bradley, E. F. 1971 Flux-profile relationships in the atmospheric surface layer. *J. Atmos. Sci.* **28**, 181–189.

Deardorff, J. W. 1970*a* A numerical study of three-dimensional turbulent channel flow at large Reynolds number. *J. Fluid Mech.* **41**, 453–480.

Deardorff, J. W. 1970*b* Convective velocity and temperature scales for the unstable planetary boundary layer and for Raleigh convection. *J. Atmos. Sci.* **27**, 1211–1213.

Deardorff, J. W. 1972 Numerical investigation of neutral and unstable planetary boundary layers. *J. Atmos. Sci.* **29**, 91–115.

Deardorff, J. W. 1973 The use of subgrid transport equations in a three-dimensional model of atmospheric turbulence. *J. Atmos. Sci.* **95**, 429–438.

Gal-Chen, T. & Wyngaard, J. C. 1982 Effects of volume averaging on the line spectra of vertical velocity from multiple-Doppler radar observations. *J. Appl. Met.* **21**, 1881–1890.

Hibberd, M. F. & Sawford, B. L. 1994 A saline laboratory model of the planetary convective boundary layer. *Boundary-Layer Met.* **67**, 229–250.

Högström, U. 1990 Analysis of turbulence structure in the surface layer with a modified similarity formulation for near neutral conditions. *J. Atmos. Sci.* **47**, 1949–1972.

Hunt, J. C. R. 1984 Turbulence structure in thermal convection and shear-free boundary layers. *J. Fluid Mech.* **138**, 161–184.

Hunt, J. C. R. & Graham, J. M. R. 1978 Free-stream turbulence near plane boundaries. *J. Fluid Mech.* **84**, 209–235.

Hunt, J. C. R., Kaimal, J. C. & Gaynor, J. E. 1988 Eddy structure in the convective boundary layer – new measurements and new concepts. *Q. J. R. Met. Soc.* **114**, 827–858.

Kader, B. A. & Yaglom, A. M. 1990 Mean fields and fluctuation moments in unstably stratified turbulent boundary layers. *J. Fluid Mech.* **212**, 637–662.

Kaimal, J. C. 1978 Horizontal velocity spectra in an unstable surface layer. *J. Atmos. Sci.* **35**, 18–24.

Kaimal, J. C., Wyngaard, J. C., Haugen, D. A., Coté, O. R., Izumi, Y., Caughey, S. J. & Readings, C. J. 1976 Turbulence structure in the convective boundary layer. *J. Atmos. Sci.* **33**, 2152–2169.

Kaimal, J. C., Wyngaard, J. C., Izumi, Y. & Coté, O. R. 1972 Spectral characteristics of surface-layer turbulence. *Q. J. R. Met. Soc.* **98**, 563–589.

Mason, P. J. & Thomson, D. J. 1992 Stochastic backscatter in large-eddy simulations of boundary layers. *J. Fluid Mech.* **242**, 51–78.

Moeng, C.-H. 1984 A large-eddy simulation model for the study of planetary boundary-layer turbulence. *J. Atmos. Sci.* **41**, 2052–2062 (referred to herein as M84).

Moeng, C.-H. & Wyngaard, J. C. 1984 Statistics of conservative scalars in the convective boundary layer. *J. Atmos. Sci.* **41**, 3161–3169.

Moeng, C.-H. & Wyngaard, J. C. 1988 Spectral analysis of large-eddy simulations of the convective boundary layer. *J. Atmos. Sci.* **45**, 3573–3587.

Monin, A. S. & Obukhov, A. M. 1954 Basic laws of trubulent mixing in the ground layer of the atmosphere. *Tr. Geofiz. Inst. Akad. Nauk SSSR* **151**, 163–187.

Obukhov, A. M. 1946 Turbulence in an atmosphere with inhomogeneous temperature. *Trans. Inst. Teoret. Geofiz. Akad. Nauk SSSR* **1**, 95–115.

Oncley, S. P., Horst, T. W., Praskovsky, A. & Wilczak, J. M. 1995 The TKE budget from the FLAT experiment. *11th Symp. on Boundary Layers and Turbulence*. American Met. Soc., Boston.

Panofsky, H. A., Tennekes, H., Lenschow, D. H. & Wyngaard, J. C. 1977 The characteristics of turbulent velocity components in the surface layer under convective conditions. *Boundary-Layer Met.* **11**, 355–361.

Paulson, C. A. 1970 The mathematical representation of wind speed and temperature profiles in the unstable atmospheric surface layer. *J. Appl. Met.* **9**, 857–861.

Peltier, L. J., Wyngaard, J. C., Khanna, S. & Brasseur, J. G. 1996 Spectra in the unstable surface layer. *J. Atmos. Sci.* **53**, 49–61.

Schmidt, H. & Schumann, U. 1989 Coherent structure of the convective boundary layer derived from large-eddy simulations. *J. Fluid Mech.* **200**, 511–562.

Sullivan, P. P., McWilliams, J. C. & Moeng, C.-H. 1994 A subgrid-scale model for large-eddy simulation of planetary boundary-layer flows. *Boundary-Layer Met.* **71**, 247–276 (referred to herein as SMM94).

Willis, G. E. & Deardorff, J. W. 1974 A laboratory model of the unstable planetary boundary layer. *J. Atmos. Sci.* **31**, 1297–1307.

Wyngaard, J. C. 1988 Planetary boundary layer. In *Lectures on Air Pollution Modeling* (ed. A. Venkatram & J. C. Wyngaard. American Met. Soc.

Wyngaard, J. C. 1992 Atmospheric turbulence. *Ann. Rev. Fluid Mech.* **24**, 205–233.

Wyngaard, J. C. & Coté, O. R. 1971 The budgets of turbulent kinetic energy and temperature variance. *J. Atmos. Sci.* **28**, 190–201.

Wyngaard, J. C. & Coté, O. R. 1972 Cospectral similarity in the atmospheric surface layer. *Q. J. R. Met. Soc.* **98**, 590–603.

Wyngaard, J. C., Coté, O. R. & Izumi, Y. 1971 Local free convection, similarity, and the budgets of shear stress and heat flux. *J. Atmos. Sci.* **28**, 1171–1182.

Wyngaard, J. C. & Peltier, L. J. 1995 Towards a dynamic drag law. *Tenth Symp. on Turbulent Shear Flows, Pennsylvania State University.*